High temperature and pressure rheological experiments on felsic granulite

D.-P. Wen[1], Y.-F. Wang[1,2]*, J.-F. Zhang[1,2], P.-X. Li[1†] and Z.-M. Jin[1,2]

[1] School of Earth Sciences and State Key Laboratory of Geological Processes and Mineral Resources, China University of Geosciences, Wuhan 430074, China

[2] Global Tectonic Center, School of Earth Sciences, China University of Geosciences, Wuhan 430074, China

*Corresponding author: Y.-F. Wang (yfwang@cug.edu.cn)

[†] Present Address: Geological Exploration Institute of Henan, Zhengzhou 450000, China

Key Points:

- The rheology of felsic granulite can be described by $\dot{\varepsilon} = 10^{-4.4\pm0.2}\sigma^{4.2\pm0.1}\exp[-(260\pm30)/(RT)]$.
- Dislocation creep dominates the deformation of granulite and its component minerals.
- Our data favor delamination-induced decratonization of the North China Craton.

Abstract

Rheological properties of continental lower crust (CLC) are essential for understanding many geodynamical processes in the Earth. Here we performed a series of deformation experiments on synthetic felsic granulite (65% plagioclase + 15% quartz + 9% clinopyroxene + 6% orthopyroxene + 5% amphibole) using a 5 GPa modified Griggs-type deformation apparatus at 827-927 °C and 1 GPa. All experiments reached a steady-state creep at strain rates ranging from 3.0×10^{-6} s^{-1} to 1.0×10^{-4} s^{-1}, yielding a stress exponent of 4.2 ± 0.1, a pre-exponential factor of $10^{-4.4\pm0.2}$ $MPa^{-4.2}$ s^{-1}, and an activation energy of 260 ± 30 kJ/mol. Microstructural observations show that plagioclase and pyroxene in deformed samples develop noticeable intracrystalline plasticity and shape preferred orientation (SPO). Electron backscatter diffraction (EBSD) measurements demonstrate more significant crystallographic preferred orientations (CPOs) of pyroxene and plagioclase in deformed granulites compared to those in hot-pressed ones. By contrast, quartz develops nearly random fabrics probably due to the simultaneous activation of multiple slip systems during deformation. These features indicate that dislocation creep dominates the deformation of these minerals and felsic granulite, consistent with the obtained stress exponent. Our data imply that a CLC consisting of felsic granulite is weaker rheologically compared to the quartz-dominated upper crust and the olivine-dominated uppermost mantle, which supports the ‘jelly sandwich’ model for the strength of continental lithosphere. Additionally, extrapolations of flow laws of our felsic granulite and formerly-reported mafic granulite strongly favor the hypothesis of delamination-induced decratonization of the North China Craton.

1. Introduction

The continental lower crust (CLC) represents where extensive mass and energy exchanges between the upper crust and the uppermost mantle occur. Rheological property of the CLC is an important parameter that concerns the interpretation of many geological processes and phenomena in the deep Earth, such as delamination and underplating (e.g., Meissner & Mooney, 1998), surface topography (e.g., Bendick et al., 2008), lower-crustal earthquakes (e.g., Reyners et al., 2007; Shi et al., 2018), seismic lamination and anisotropy of the CLC (e.g., Meissner et al., 2006; Ross et al., 2004; Shapiro et al., 2004), and coupling and decoupling of crust and mantle (e.g., Royden, 1996). Understanding the rheological properties of CLC is thus fundamental to fully decipher the geodynamics of the Earth.

There are, however, still hot debates regarding the rheology of CLC. Some researchers suggest that the CLC is mechanically weaker than the upper mantle and the upper crust (i.e., the "jelly sandwich" model) (e.g., Chen & Molnar, 1983), while some argue that the strength of continental lithosphere resides entirely in the crust and that the upper mantle is significantly weaker compared to the CLC [i.e., the "crème brûlée" model (Burov & Watts, 2006)] (e.g., Jackson, 2002; see Bürgman & Dresen, 2008 for a review). Both hypotheses find supports from many geophysical and geodetic observations and numerical modellings (e.g., Beaumont et al., 2001; Clark et al., 2005; Copley et al., 2011; Ross et al., 2004; Royden et al., 1997). These disputes arise, on the one hand, due to the variety of rheology in response to heterogeneous lithologies and thermodynamic conditions, including temperature and fluid, in the CLC. On the other hand, geophysical and geodetic techniques usually give non-unique, qualitative but not quantitative constraints on the mechanical properties of the CLC. In contrast to these inferences generally deduced from natural observations, laboratory experiments on representative CLC rocks under controlled thermodynamic conditions allow us to resolve these disputes in a more

straightforward way.

Based on studies on exposed lower crustal sections and basalt-borne lower crustal xenoliths and seismic velocities of the CLC, it is generally suggested that the CLC is intermediate to mafic in bulk composition (Gao et al., 1998; Rudnick & Fountain, 1995; Rudnick & Gao, 2003). A recent review (Hacker et al., 2015), however, argues that much of the CLC is relatively felsic instead. Whatever the bulk composition is, mafic/felsic granulites are commonly observed as an important rock type in lower crustal sections and xenoliths (e.g., Chen et al., 2006; Franěk et al., 2011; Griffin & O'Reilly, 1986; Martelat et al., 1999). Therefore, a thorough knowledge of rheology of the CLC requires an understanding of the mechanical behavior of mafic/felsic granulites. Only a few studies have touched the rheology of granulites up to now, in stark contrast to numerous studies on the proxy of the upper mantle, i.e. olivine (see a review by Hirth & Kohlstedt, 2003). Wilks and Carter (1990) first investigated the rheology of CLC through experiments on selected natural mafic and felsic granulites. Unfortunately, due probably to the coarse-grained (» 100 μm) nature of their samples, most of their experiments show semibrittle to cataclastic behavior and do not reach steady-state creep. Therefore, these results cannot be reliably extrapolated to nature. Recently, Wang et al. (2012) performed experiments on synthetic mafic granulites using a 3 GPa modified Griggs-type apparatus, which greatly improves the precision of measured stress level with molten salt as the confining pressure medium. They showed that the steady-state creep strength of the studied mafic granulite is weaker than olivine aggregates, and thus supports the "jelly sandwich" model of the continental lithosphere strength envelope.

Since pyroxene and plagioclase are the most common minerals that make up the CLC, many studies have alternatively made efforts to determine the flow laws of pyroxene and/or plagioclase aggregates under various thermodynamic conditions (e.g.,

Bystricky & Mackwell, 2001; Dimanov & Dresen, 2005; Dimanov et al., 1999, 2003; Rybacki & Dresen, 2000; Rybacki et al., 2006) to understand the rheology of CLC. Theoretically, these single-phase flow laws can be used to reasonably deduce the flow law of a multiphase aggregate that is made up of these phases (e.g., Ji et al., 2003; Tullis et al., 1991). Nevertheless, this application is generally limited by the facts that 1) the deformation mechanism for each component mineral may not be the same or may change with progressive deformation, especially when dynamic recrystallization occurs; 2) possible reactions may happen between the component minerals; and 3) mechanical anisotropy is not taken into account in such theoretical models. Therefore, a direct experimental study on granulite is necessary.

In that the constitutive equation for a synthetic mafic granulite (Wang et al., 2012) has been established recently, we therefore aim to determine in this study the rheological parameters of felsic granulite under conditions appropriate to the CLC. To overcome the limitations of previous experiments on natural felsic granulites by Wilks and Carter (1990), we used synthetic fine-grained (32-53 μm) felsic granulites, which have been well characterized in terms of water concentrations and chemical compositions of the major component minerals, as experimental samples. In addition, the deformation apparatus used in this study improves greatly the accuracy of stress measurement during deformation compared to the one used in Wilks and Carter (1990) by using molten salt as the confining pressure medium (Green & Borch, 1989).

2. Experimental Samples and Methods

2.1. Starting Material

As starting material, we used a natural, fresh felsic granulite (09TPZ-1) collected from Taipingzhai in the Archean lower crust terrane of the North China Craton (NCC). This felsic granulite is primarily composed of 65% plagioclase, 15% quartz, 9% clinopyroxene, 6% orthopyroxene, and 5% amphibole, with accessory K-feldspar and

ilmenite. P-T estimates using major element- and REE-based thermobarometers yielded a temperature of 1025-1060 ºC and a pressure of 0.9 GPa for the clinopyroxene-orthopyroxene pair in the Taipingzhai granulites (Yang & Wei, 2017). Mineral separates were prepared using heavy liquid and magnetic separation and then ground to fine powders using a tungsten carbide mortar. These powders were then sorted to a desired grain size of 32-53 μm using a sedimentation method based on the Stokes' law of settling. The sorted powders were subsequently well mixed in terms of the modal composition of the staring material. Prior to being loaded into sample capsules, the powders were dried in a drying oven at 100 ºC for more than 48 hours to remove possible absorbed water.

2.2. Deformation Apparatus and Experiments

All experiments were performed in a 5 GPa modified Griggs-type apparatus at the State Key Laboratory of Geological Processes and Minerals Resources, China University of Geosciences (Wuhan) (GPMR-CUG). Sample assembly and preparation procedure used in this study generally followed those detailed in Zhang and Green (2007) and Wang et al. (2012), except that a slight modification to the sample dimension (3.2 mm ID instead of 3.0 mm ID) was made in this study. The sample assemblies were kept in a drying oven at 100 ºC for > 12 h before they were put into the high-pressure apparatus. Constant piston-velocity deformation experiments were carried out at a pressure of 1 GPa and temperatures of 827-927 ºC immediately following a hot-pressing of the powder sample under 1 GPa and 927 ºC conditions for 12 h. For those experiments not performed at 927 ºC, load was not applied until temperature was adjusted to the desired value and kept for 1 h while maintaining the confining pressure constant. To determine the initial sample length and microstructures for each deformation experiment, three hot-pressing experiments were performed separately under 1 GPa and 927 ºC conditions for 12 h. At the end of each experiment, temperature was quenched to 300 ºC within a few seconds to retain

the microstructures. Experimental temperatures are measured to a precision of 1 ºC using the thermocouple located near the top of the sample. This thermocouple generally gives higher (up to 25 ºC) temperature readings than that located near the bottom of the sample. Data of pressure, temperature, load, strain rate, and displacement were recorded automatically every 10 seconds by a computer.

2.3. Mineral Composition Analyses

To examine whether any modifications to chemical compositions occur during experiments, we measured the major-element compositions of component minerals in the starting material and the hot-pressed and deformed samples by a JEOL JXA-8230 electron probe microanalyser (EPMA) at the Center for Global Tectonics, School of Earth Sciences, China University of Geosciences (Wuhan). The analyses were conducted at an accelerating voltage of 15 kV, a probe current of 20 nA, and a beam size of 3 μm. Dwell times were 10 s on element peaks and 5 s on background locations adjacent to peaks. Raw X-ray intensities were corrected using a ZAF correction procedure. Natural and synthetic SPI standards were used as monitor standards: sanidine for K, pyrope for Fe and Al, diopside for Ca and Mg, jadeite for Na, rhodonite for Mn, olivine for Si, and rutile for Ti. Furthermore, we also collected semi-quantitative X-ray mineral chemical mapping of deformed samples using an energy-dispersive spectrometer mounted on a Quanta 450 field emission gun scanning electron microscopy (SEM) at GPMR-CUG.

2.4. Microstructural Characterization

Thin sections and/or polished sections were prepared by cutting the experimental specimens longitudinally and polishing to within 0.05 μm using colloidal alumina. Microstructures of hot-pressed and deformed samples were examined by a petrographic microscope and the SEM at GPMR-CUG. Crystallographic preferred orientation (CPO) of minerals were determined by an Oxford Instruments Nordlys-II

electron backscatter diffraction (EBSD) system at GPMR-CUG. To reveal the intracrystalline deformation features, we also performed EBSD mapping on selected grains from deformed samples. The measurements were carried out with an accelerating voltage of 20 kV, a spot size of 6, and a working distance of 23-25 mm. Diffraction patterns were manually collected and indexed using the Channel 5 + software. Only those measurements with mean angular deviation (MAD) values below 1.0 (between detected and simulated Kikuchi bands) were recorded. The strength of CPO is quantified by the misorientation index (M-index) developed by Skemer et al. (2005) and the J-index using the program of *SuperJctfPC.exe* courtesy of David Mainprice. The M-index is 0 for a random fabric and 1 for a single crystal, while the J-index is 1 for a random distribution and infinity for a single crystal orientation.

2.5. Fourier Transform Infrared (FTIR) Analyses

To determine the initial water concentrations of minerals in the experimental samples, we prepared a thick section of 225 μm thickness by doubly polishing a rock slab randomly cut from the natural sample (09TPZ-1). Unpolarized FTIR spectroscopic measurements were taken at GPMR-CUG on a Nicolet 6700 spectrometer coupled with a Continuμm IR microscope using a KBr beam splitter and a liquid-nitrogen cooled MCT-A detector. 128 scans were accumulated for each spectrum with a resolution of 4 cm^{-1}. Depending on grain size, the aperture size was set to be 50 × 50 μm to 100 × 100 μm. Measurements were made on optically clean, crack- and inclusion-free regions. More than 10 different grains for each mineral were analyzed. Water concentrations were calculated using a modified form of the Beer-Lambert law

$$c = \Delta / (I \times t)$$

where c is the water concentration (ppm H_2O by weight), Δ is the integrated area (cm^{-1}) of absorption bands in the region of interest, t is the sample thickness (cm), and I is the integral specific absorption coefficient (ppm^{-1} cm^{-2}). For each spectrum,

baseline correction was manually performed and the OH absorption bands were integrated between 3000 and 3800 cm^{-1}. The obtained area beneath the OH peaks was multiplied by 3 to give the Δ values. The integral specific absorption coefficients of 7.09 ppm^{-1} cm^{-2} for clinopyroxene (Bell et al., 1995), 14.84 ppm^{-1} cm^{-2} for orthopyroxene (Bell et al., 1995), 13.50 ppm^{-1} cm^{-2} for quartz (Thomas et al., 2009), and 15.30 ppm^{-1} cm^{-2} for plagioclase (Johnson & Rossman, 2003) were used. The thickness of the thick section was measured using a digital micrometer and reported as an average of 10 measurements covering the whole section. The uncertainties arising from use of an unpolarized IR beam on unoriented anisotropic minerals can be minimized by measurements on more than ten different grains of each mineral (e.g., Kovács et al., 2008; Withers, 2013).

3. Results

3.1. Experimental Results

The three hot-pressing experiments yield quite similar axial compression ratio, ranging between 35% and 38% (Table 1). The retrieved hot-pressed and deformed samples remain nearly cylindrical in shape (Figure 1). Measurements on one of the hot-pressed samples show that it has a density of 3.14 g/cm^3 and a porosity of ~ 1%.

At high temperatures and pressures, a power-law creep often dominates the plastic deformation of rocks. The constitutive relation is well described by an empirical equation of the form:

$$\dot{\varepsilon} = \mathrm{A}\sigma^{n} \exp[-Q/\mathrm{R}T]$$

where $\dot{\varepsilon}$ is the strain rate, A is the pre-exponential factor related with material, σ is the steady-state flow stress, n is the stress exponent related to deformation mechanism (n = 3-5 for dislocation creep and n = ~1 for diffusion creep), Q is the activation energy, R is the gas constant, and T is the absolute temperature. 10 deformation experiments (Table 1) in total have been carried out at a confining pressure of 1 GPa

to determine the rheological parameters for the studied felsic granulite. Representative stress versus strain curves are illustrated in Figure 2a, which shows that a steady-state deformation generally reaches after a strain of about 20%. The deformation experiments can be classified into two groups: one group is performed at constant temperature but varying strain rates of 3.6×10^{-6} s^{-1}, 1.1×10^{-5} s^{-1}, 9.4×10^{-5} s^{-1}, respectively, while the other group is performed at constant strain rate but varying temperatures of 827 ºC, 877 ºC, and 927 ºC, respectively. As shown in Figure 2b, a log-log plot of strain rate versus stress for the first group of experiments yields a stress exponent of $n = 4.2 \pm 0.1$ and a pre-exponential factor of $A = 10^{-4.4\pm0.2}$ $MPa^{-4.2}$ s^{-1}. The creep activation energy was determined to be 260 ± 30 kJ/mol using least square fits based on the second group of experiments (Figure 2c). The rheology of felsic granulite over the range of conditions explored here can thus be described by the following constitutive equation:

$$\dot{\varepsilon} = 10^{-4.4\pm0.2}\mathrm{MPa}^{-4.2}\mathrm{s}^{-1}\sigma^{4.2\pm0.1}\exp\left(-\frac{260\pm30\ \mathrm{kJ/mol}}{RT}\right)$$

where $\dot{\varepsilon}$ is in s^{-1}, σ in MPa, and T in Kelvin.

3.2. Microstructures

Under petrographic microscope and SEM, the hot-pressed samples show nearly homogeneous distribution of each component mineral; no compositional layering or single-phase clusters have been observed (Figures 3a and 3b). A weak shape preferred orientation (SPO) as shown by the partial alignment of anisometric pyroxene and amphibole grains (Figures 3a and 3b) can be discerned. EBSD results show that all minerals from the hot-pressed samples have very weak CPOs (Figure 4a). Pyroxene CPOs are similar, featured by the [100]-axis approximately parallel to while the [001]-axis nearly normal to the compression direction. Although being more diffused, the [100]-axis of plagioclase grains appear to be nearly normal to the compression direction. The *c*-axes of quartz form two weak, broad point maxima with one nearly normal to and the other oblique at an angle of ~ 45° to the compression direction.

In contrast to the hot-pressed samples, the deformed samples developed more significant SPO manifested by the strong alignment of elongate pyroxene, amphibole, plagioclase and sometimes quartz (Figures 3c and 3d), which also defines the foliation plane in deformed samples. Undulose extinction is frequently observed in plagioclase and quartz. EBSD mappings show that subgrain structures are common in plagioclase, pyroxene and quartz (Figure 5). Due probably to low finite strain ($\varepsilon < 50\%$; Table 1), mineral CPOs in the deformed samples are still weak. However, pyroxene and plagioclase CPOs in the deformed samples are stronger than their counterparts in the hot-pressed samples (Figure 4). Pyroxene CPOs are characterized by a clear point maximum of the [100]-axis nearly normal to the foliation plane and a great girdle of the [001]-axis nearly parallel to the foliation plane. The [100] axes of plagioclase form a girdle in the foliation plane, while poles to the (001)-plane concentrate approximately normal to the foliation plane. The quartz CPOs are nearly random with J-index ranging from 2.82 to 3.44 (Figures 4b-c).

Finally, it is noteworthy that the phase boundaries and triple junctions among the component minerals in deformed samples are clear-cut and devoid of any amorphous phases (i.e., melt), even at high magnifications (Figure 6).

3.3. Chemical Composition and Water Concentration

The major-element compositions of minerals in the starting material and selected hot-pressed and deformed samples are shown in Table 2. Compared to the staring material, no significant compositional change occurs during hot-pressing and deformation. In addition, X-ray maps of Si, Al, Fe, Mg and Ca show no discernable compositional zoning in each mineral and sharp grain/phase boundaries (Figure 7).

Figure 8 illustrates the typical infrared spectra for plagioclase, quartz, clinopyroxene,

and orthopyroxene from the starting material. All spectra are normalized to 1 cm thickness and offset vertically for clarity. A summary of FTIR results is listed in Table 3. Most FTIR spectra of plagioclase are characterized by two absorption bands (Figure 8a): a strong sharp band at 3620 cm^{-1} and a broad band centered around 3440 cm^{-1}, which may be related to structural OH or water molecule (Johnson & Rossman, 2004). The calculated water concentrations in plagioclase vary considerably, ranging from 17-400 wt ppm with an average of 209 ± 126 wt ppm (Table 3). Infrared spectra of quartz are consistently similar and characterized by the presence of two small sharp peaks at 3380 cm^{-1} and 3440 cm^{-1} superimposing on a broad band at 3400 cm^{-1} (Figure 8b). The sharp peaks are generally attributed to structurally bound hydrogen associated with Al^{3+} or monovalent cations (Aines & Rossman, 1984; Johnson, 2006), while the broad band is considered to be due to the O-H stretching vibrations of "liquid-like" molecular water (e.g., Aines & Rossman, 1984; Ito & Nakashima, 2002; Kronenberg & Wolf, 1990; Nakashima et al., 1995). Quartz contains an average water concentration of 355 ± 127 wt ppm (Table 3). Clinopyroxene displays significant absorption bands at 3620 cm^{-1}, 3530 cm^{-1}, and 3450 cm^{-1}, with intensity of 3620 cm^{-1} generally being the strongest (Figure 8c). Such bands are analogous to those reported by previous studies for clinopyroxene and commonly considered as structural OH (e.g., Peslier et al., 2002; Rossman, 1996; Skogby et al., 1990; Xia et al., 2006; Yang et al., 2008). The calculated average water concentration in clinopyroxene is 937 ± 521 wt ppm (Table 3). The most prominent feature of the FTIR spectra in orthopyroxene is a stronger sharp absorption band at around 3620-3605 cm^{-1} accompanied by two weaker, broad bands at 3430-3415 cm^{-1} and 3250-3235 cm^{-1}, respectively (Figure 8d). These bands are related to structural OH in orthopyroxene and have been frequently reported by previous studies (e.g., Skogby et al., 1990; Xia et al., 2006; Yang et al., 2008). The average water concentration is 1132 ± 555 wt ppm in orthopyroxene (Table 3). According to mineral mode and measured water concentration in each component mineral, the studied felsic granulite thus has a bulk

water concentration of 344 ± 182 wt ppm, excluding the contribution of amphibole. This value falls within the range reported previously for granulites from the eastern China (Xia et al., 2006; Yang et al., 2008).

4. Discussion

4.1. Deformation Mechanism(s)

Owing to being volumetrically predominant, plagioclase should govern the rheological behavior of the studied felsic granulite. Microstructural observations showed that plagioclase in deformed samples developed distinct SPO (Figure 2d), which is nearly normal to the compressive stress direction. EBSD analyses on deformed samples illustrated that plagioclase has significant intracrystalline plasticity (Figure 5a) and stronger CPOs (Figures 4b-d). These facts suggest that dislocation creep is the dominant deformation mechanism in plagioclase, consistent with the dislocation-creep deformation of the felsic granulite as indicated by the stress exponent of 4.2 ± 0.1. In general, the dominant slip system during dislocation-creep deformation of a mineral can be deduced from its CPO. Strictly speaking, this practice is inapplicable to mineral deformation by axial compression (like in this study) as only the slip plane can be unambiguously determined. Nevertheless, for those low-symmetry crystal system minerals, like plagioclase and pyroxene, the most probable slip direction can generally be inferred if the slip plane is determined, because the common slip systems in these minerals are well known and limited in number. In this study, the CPO patterns of deformed plagioclase are characterized by both the [100]-axis and the (001)-plane subparallel to the foliation plane, suggesting that (001)-plane is the slip plane with [100]-axis being the most probable slip direction, i.e., the (001)[100] slip system. Such a slip system has been frequently inferred to be activated during dislocation creep of plagioclase in naturally and experimentally deformed rocks (e.g., Heidelbach et al., 2000; Ji et al., 2004; Mehl & Hirth, 2008; Wang et al., 2012; Xie et al., 2003).

Microstructural observations showed that pyroxene has distinct SPO being consistent with that of plagioclase. EBSD analyses revealed significant intracrystalline plasticity and enhanced CPOs in pyroxene after deformation (Figures 4b-d, 5b, and 5c). The CPOs of pyroxene, featured by a point maximum of [100]-axis nearly normal to the foliation and a girdle distribution of [001]-axis nearly parallel to the foliation, point to a dominant slip system of (100)[001]. This slip system is commonly reported to be the one in experimentally and naturally deformed pyroxene by a dislocation-creep deformation (e.g., Farla et al., 2017; Lund et al., 2006; Mauler et al., 2000; Wang et al., 2012; Zhang & Green, 2007). These observations suggest that dislocation creep controls the deformation of pyroxene, which is in agreement with the dislocation-creep deformation of the felsic granulite as well.

Quartz in deformed samples shows weak SPO and nearly random fabrics. Such features may be interpreted as deformation by grain boundary sliding or diffusion creep. However, these deformation mechanisms do not involve significant intracrystalline plasticity, which is inconsistent with the observed undulose extinction and intracrystalline misorientation in quartz (Figure 5d). In addition, since Si is the slowest diffusing species in quartz, the diffusion of Si will thus be the rate-limiting factor in diffusion creep of quartz. Based on the Arrhenius equation for Si diffusion compiled by Cherniak (2010), we estimated the time required to diffuse Si for 15 μm (i.e., the radius of the smallest quartz grains) at a temperature of 927 ºC. Our estimation suggests that the required time is far beyond that of the experimental timescale, indicating that intracrystalline diffusion creep is impossible in our experiments. The absence of fluid or melt along grain boundaries does not favor the operation of grain boundary diffusion creep either, which is identical with the lack of chemical zoning in each mineral (Figure 7).

Alternatively, the nearly random CPO of quartz can be ascribed to its small volume fraction (15%) in the samples, which is not enough to form a stress-supporting framework, and the dispersion of quartz grains between those of strong minerals such as plagioclase and clinopyroxene. However, pyroxene in our samples has also a low volume fraction (15%) and is well mixed with other minerals. If the above hypothesis is valid, then it is expected to see nearly random fabrics of pyroxene too. This is obviously not the case—pyroxene in our deformed samples shows well-defined CPO patterns (Figure 4b-d). In addition, as had been demonstrated in natural observations (Martelat et al., 1999), even if quartz does not form a stress-supporting framework, it can still develop non-random CPOs. Zhang and Green (2007) conducted deformation experiments at 927-1227 ºC on quartz eclogites. Their data show that quartz develops distinct SPO but no significant CPOs. The authors suggested that multiple slip systems were activated for quartz during deformation, leading to weak to random CPOs. We consider that this hypothesis may well account for the random quartz CPOs in our study. Therefore, dislocation creep dominates the deformation of quartz as well, which is consistent with the observed intracrystalline plasticity in quartz.

In a word, our mechanical data and microstructural observations point to dislocation creep as the dominant deformation mechanism in the deformed felsic granulite and its major component minerals.

4.2. Comparison with Previous Studies

Since plagioclase is the primary component mineral in the studied felsic granulite and commonly considered to be representative of the CLC in terms of rheology, it is thus interesting to compare the rheological strength of our felsic granulite with that of plagioclase in the dislocation-creep regime. Prior to this discussion, however, it is necessary to address whether water in our samples has been lost during deformation experiments. Considering that H has an elevated mobility at high temperatures and

414 can go through the platinum capsule easily (e.g., Wilks et al., 1990), it must have been
415 partially lost during experiments. However, an accurate determination of water
416 concentrations of minerals after deformation is hampered due to the following two
417 reasons. First, the grain sizes (32-53 μm) of minerals in our experimental samples are
418 very small. In particular, compression- and decompression-induced microcracks are
419 common in many grains (Figure 6). These facts make measurements of water
420 concentrations within each mineral after experiments using a conventional FTIR,
421 which is usually applied with an aperture size of ≥ 50 μm, impractical. Second,
422 although the secondary ion mass spectrometry (SIMS) technique has a better spatial
423 resolution (5-10 μm; e.g., Huari et al., 2002) than a conventional FTIR, its application
424 is currently restricted by lacking suitable standards, especially for plagioclase and
425 quartz. However, as suggested below, water loss from our experimental samples must
426 be minimal.
427
428 In addition, it is important to notice that the dominant slip system {i.e., the (001)[100]
429 slip system} in plagioclase in this study differs from the one that has been commonly
430 identified based on TEM observations and CPOs of plagioclase from naturally
431 deformed middle-lower crustal rocks (e.g., Ji & Mainprice, 1988, 1990; Kruse et al.,
432 2001; Miranda & Klepeis, 2016; Montardi & Mainprice, 1987; Olsen & Kohlstedt,
433 1984; Svahnberg & Piazolo, 2010). Ji et al. (2000, 2004) proposed that the relative
434 importance of the [001] or [100] Burgers vectors may be a function of temperature,
435 strain rate, water activity or confining pressure. In particular, water is potentially the
436 most important parameter that may influence the slip system transitions in plagioclase,
437 considering that the range of temperature and pressure conditions in the middle-lower
438 crust is limited. Laboratory experiments (Jung & Karato, 2001; Manthilake et al.,
439 2013; Ohuchi et al., 2012) have clearly shown that, at least for olivine and
440 orthopyroxene, water concentration in these minerals has a pronounced influence on
441 the dominant slip system and their CPOs. The water concentration in plagioclase from

442 the lower crustal rocks can vary significantly from several tens to nearly one thousand
443 wt ppm (e.g., Xia et al., 2006; Yang et al., 2008). However, how water concentration
444 may influence the activity of these slip systems in plagioclase remains largely
445 unknown due to lack of experimental constraints. Moreover, information about the
446 water concentration in plagioclase from previous studies on naturally deformed
447 middle-lower crustal rocks is generally lacking, thus making the discussion of the
448 relative activity and strength of the (010)[001] and (001)[100] slip systems in
449 plagioclase inappropriate.
450
451 When extrapolated to a natural strain rate of 10^{-14} s^{-1}, our felsic granulite is more than
452 3 times weaker than dry anorthite (Rybacki et al., 2006) under the lower-crustal
453 temperature (800-900 ºC) conditions (Figure 9a). Because the presence of water can
454 significantly reduce the mechanical strength of minerals and rocks (e.g., Chen et al.,
455 2006; Griggs & Blacic, 1965; Hirth & Kohlstedt, 2003; Mei & Kohlstedt, 2000; Wang
456 et al., 2012) and plagioclase in our starting material contains a water concentration of
457 ~ 0.021 wt% H_2O (Table 3), it is thus no wonder that our felsic granulite is
458 significantly weaker than the dry anorthite aggregates (Rybacki et al., 2006). In
459 addition, FTIR results show that quartz (15%), clinopyroxene (9%) and
460 orthopyroxene (6%) in the studied felsic granulite all contain a large amount of water
461 (Table 3). Extrapolations of published dislocation-creep flow laws for these minerals
462 under wet conditions (Bystricky et al., 2016; Chen et al., 2006; Rutter et al., 2004)
463 (Figure 7a) reveal that quartz and clinopyroxene are both much weaker while
464 orthopyroxene is slightly stronger than dry anorthite. Hence, the net effects of these
465 minor minerals also tend to drive the felsic granulite weaker than the dry anorthite.
466 Using the flow law for dislocation creep of anorthite under hydrous conditions
467 (Rybacki et al., 2006), we also calculated the flow strength of wet anorthite (0.02 wt%
468 H_2O) as a function of temperature at a strain rate of 10^{-14} s^{-1} (Figure 9a). It is clear
469 from Figure 9a that our felsic granulite is only slightly (up to nearly 2 times) stronger

than wet anorthite at 800-900 ºC. Such a small strength contrast implies that hydrogen diffusional loss from the component minerals during deformation, if any, must be insignificant. Alternatively, this strength contrast could be attributed to the combined effects of quartz and pyroxene, which are respectively weaker and stronger than the wet anorthite (Figure 9a), if we assume that the influence of anorthite content in plagioclase on rheology is negligible.

In Figure 9b, we also compare the rheological strength of our felsic granulite with those of granulites reported by previous studies by extrapolation to a natural strain rate of 10^{-14} s^{-1}. It is clear that our felsic granulite is 6-7 times stronger than the Adirondack felsic granulite (Wilks & Carter, 1990), but comparable to that of the amphibole-rich Pikwitonei mafic granulite (Wilks & Carter, 1990) at 800-900 ºC. However, the reason behind the similarities and differences of the strength between our sample and those of Wilks and Carter (1990) is difficult to address currently due to significantly different mineralogy [65% Pl + 15% Py + 15% Qz + 5% Amp in this study versus 45% Kfs + 21% Qz + 20% Cpx + 1% Pl + 1% Amp and 58 Hbl + 40% Pl + 1% Cpx + 1% Opx for felsic and mafic granulite, respectively, in Wilks and Carter (1990)]. Furthermore, water concentrations in minerals from granulites studied by Wilks and Carter (1990) are unstated, which renders such a discussion impossible as well.

Compared with the mafic granulite (57% Pl + 14% Opx + 24% Cpx + 5% Opq) studied by Wang et al. (2012), the felsic granulite studied here is much (6-7 times) stronger (Figure 9b). At first glance, this seems unreasonable since the mafic granulite has more pyroxene which would make it stronger than the pyroxene-poor felsic granulite (Figure 9a). Two reasons could probably explain this discrepancy. First, the mafic granulites have water concentrations (0.16-0.28 wt% H_2O) far more than those (0.034 wt% H_2O) of the felsic granulites. More significant water-weakening effect

caused by more water concentrations in the mafic granulites could explain why the mafic granulites are weaker than the felsic granulites. Second, the anisometric shape of pyroxene and plagioclase grains as a result of fracturing along cleavage planes during powder preparation leads to a weak SPO (i.e., foliation) and fabric (Figures 3c, 3d and 4a) during hot-pressing, which in turn gives rise to mechanical anisotropy (e.g., Hansen et al., 2012; Ji et al., 2000) and increases the strength of the felsic granulite.

4.3. Geological Implications

Our microstructural observations, EBSD results and stress exponent (n = 4.2 ± 0.1) all point to dislocation creep as the dominant deformation mechanism in the studied felsic granulite at lower-crustal *P-T* conditions. Dislocation creep also plays an important role in the deformation of many naturally deformed lower-crustal rocks (e.g., Lund et al., 2006; Martelat et al., 1999). Therefore, the flow law of felsic granulite obtained here can be applied reliably to natural conditions.

When extrapolated to a natural strain rate of 10^{-14} s^{-1}, our felsic granulite is much stronger than wet quartz aggregates (Figure 9a), which are commonly considered to be rheologically representative of the upper crust, under the same temperature and pressure conditions. However, due to low temperature and dominantly brittle deformation, the upper crust is generally stronger than the lower crust (Bürgmann & Dresen, 2008; Kohlstedt et al., 1995; Ranalli & Murphy, 1987). In addition, dry olivine aggregates (Hirth & Kohlstedt, 2003) and eclogite (Zhang & Green, 2007), which are representative of the upper mantle and the thickened lower crust, respectively, are nearly one order of magnitude stronger than the studied felsic granulite at the Moho depth (Figure 10), even if the felsic granulite is stressed along a 'hard' direction. We also calculated the flow strength of water-saturated olivine aggregates at Moho depth (1 GPa, 900 ºC) as a function of temperature (Figure 10). The water concentration in water-saturated olivine is estimated to be ~ 57 wt ppm

526 H_2O using the solubility equation of Zhao et al. (2004). As a matter of fact, water
527 concentration in mantle olivine is generally far below its saturation level. It is obvious
528 from Figure 10 that the felsic granulite is nearly 3 times weaker than water-saturated
529 olivine aggregates at Moho. These results suggest that the felsic granulite is weaker
530 than the upper crust and the uppermost mantle, supporting the "jelly sandwich" model
531 of the continental lithosphere strength envelope (e.g., Chen & Molnar, 1983). This
532 viewpoint is consistent with that of Wang et al. (2012), and is supported by many
533 geodetic and geological observations worldwide (e.g., Homburg et al., 2010; for a
534 review, see also Bürgmann & Dresen, 2008). It is worth mentioning that this
535 viewpoint holds true only when the CLC is composed mainly of felsic granulite
536 similar in mode composition to the one studied here. However, numerous previous
537 studies have shown that the CLC is lithologically complex, with mineral species and
538 modes varying from locality to locality (e.g., Chen et al., 2006; O'Brien & Rötzler,
539 2003). This compositional variation explains in part why the "jelly sandwich" model
540 fails somewhere (e.g., Jackson, 2002) in the Earth.
541
542 As summarized by Wang et al. (2012), a weak CLC is helpful to understanding many
543 issues related to deep geodynamics, such as laminated seismic reflectors and seismic
544 anisotropy observed in the CLC (e.g., Meissner et al., 2006; Ross et al., 2004) and
545 surface topography and crustal shortening (e.g., Bendick et al., 2008; Chen et al.,
546 2017; Gerbault et al., 2005). For instance, Gerbault et al. (2005) suggested through
547 numerical modeling that horizontal flow of the lower crust from Puna towards
548 Altiplano of the central Andes driven by excess density-induced stress from the
549 Altiplano mantle could explain the different amounts of crustal shortening in
550 Altiplano and Puna. More importantly, rheology of the studied felsic granulite, which
551 samples the Archean lower crust of the NCC, is immediately applicable to and has
552 particular implications for the evolution of the NCC. Several lines of evidence have
553 proved that the NCC, one of the oldest continental nuclei in the world, had lost its

keel or the NCC had been destroyed since the Mesozoic (e.g., Fan et al., 2000; Menzies et al., 1993; Xu et al., 2001). Delamination of the thickened, eclogitic lower crust, whose existence had been inferred from many geochemical and geological evidence (e.g., Gao et al., 2004; Xu et al., 2002, 2008), and probably the lithospheric mantle has been put forward as a viable mechanism to explain the destruction of the NCC (e.g., Gao et al., 2009). In addition to gravity-triggered instability, the onset of delamination requires mechanical decoupling between the lower CLC (eclogite)/lithospheric mantle and the upper CLC (consisting mainly of granulite in the NCC) as well (Meissner & Mooney, 1998). The mafic granulite (Wang et al., 2012) and the felsic granulite studied here are nearly one to two orders of magnitude softer than eclogite (Zhang & Green, 2007; see Figure 10). This strength contrast will surely contribute to mechanical decoupling between the upper CLC and the lower CLC, which in turn favors the hypothesis of delamination-induced destruction of the NCC.

5. Conclusions

We present here high-temperature and -pressure rheological experiments on synthetic felsic granulites. We varied strain rate and temperature to determine their effects on the measured stress. Our experiments and data reduction result in a stress exponent of $n = 4.2 \pm 0.1$ and an activation energy of $Q = 260 \pm 30$ kJ/mol. Microstructural analyses revealed enhanced CPO strength of pyroxene and plagioclase in the deformed samples compared to their counterparts in the hot-pressed ones, whereas quartz CPOs become random after deformation. In addition, all these minerals display distinct intracrystalline plasticity like undulose extinction and subgrain structure. These microstructural observations combined with the obtained stress exponent indicate that deformation was dominated by dislocation creep in both the rock and the component minerals. Extrapolations of our flow law imply a weaker continental lower crust compared to the upper crust and the uppermost mantle, supporting the “jelly sandwich” continental lithosphere strength model. In particular, this conclusion favors

582 the delamination model for the destruction of the NCC.

583

584 ## Acknowledgements

585 We are grateful to Chujian Liu for fabrication of parts for sample assemblies. Thanks
586 are also due to Xiong Wang, Zhenjiang Wang, Zhonghang Wang and Jing Chen for
587 their help with sample preparation and experiments. Prof. Yi Cao and Haijun Xu are
588 thanked for helpful discussions. Constructive and insightful comments by Haemyeong
589 Jung and an anonymous reviewer are very helpful to improve the quality of the
590 manuscript and greatly thanked. This research was supported by the National Natural
591 Science Foundation of China (NSFC) (grant Nos. 41372224, 41590623, and
592 41872230). Data used in this study are available from
593 https://doi.org/10.6084/m9.figshare.9771458.v1.

594

References

Aines, R. D., & Rossman, G. R. (1984). Water in minerals? A peak in the infrared. *Journal of Geophysical Research: Solid Earth, 89*(B6), 4059-4071. https://doi.org/10.1029/JB089iB06p04059

Beaumont, C., Jamieson, R. A., Nguyen, M. H., & Lee, B. (2001). Himalayan tectonics explained by extrusion of a low-viscosity crustal channel coupled to focused surface denudation. *Nature, 414*(6865), 738-742. https://doi.org/10.1038/414738a

Bell, D. R., Ihinger, P. D., & Rossman, G. R. (1995). Quantitative analysis of trace OH in garnet and pyroxenes. *American Mineralogist, 80*(5-6), 465-474. https://doi.org/10.2138/am-1995-5-607

Bendick, R., McKenzie, D., & Etienne, J. (2008). Topography associated with crustal flow in continental collisions, with application to Tibet. *Geophysical Journal International, 175*(1), 375-385. https://doi.org/10.1111/j.1365-246X.2008.03890.x

Bürgmann, R., & Dresen, G. (2008). Rheology of the lower crust and upper mantle: Evidence from rock mechanics, geodesy, and field observations. *Annual Review of Earth and Planetary Sciences, 36*(1), 531-567. https://doi.org/10.1146/annurev.earth.36.031207.124326

Burov, E. B., & Watts, A. B. (2006). The long-term strength of continental lithosphere: "jelly sandwich" or "crème brûlée"? *GSA Today, 16*(1), 4-10. https://doi.org/10.1130/1052-5173(2006)016<4:tltsoc>2.0.co;2

Bystricky, M., Lawlis, J., Mackwell, S., Heidelbach, F., & Raterron, P. (2016). High-temperature deformation of enstatite aggregates. *Journal of Geophysical Research: Solid Earth, 121*(9), 6384-6400. https://doi.org/10.1002/2016jb013011

Bystricky, M., & Mackwell, S. (2001). Creep of dry clinopyroxene aggregates. *Journal of Geophysical Research: Solid Earth, 106*(B7), 13443-13454. https://doi.org/10.1029/2001jb000333

Chen, L., Capitanio, F. A., Liu, L., & Gerya, T. V. (2017). Crustal rheology controls on the Tibetan plateau formation during India-Asia convergence. *Nature Communications, 8*, 1-8. https://doi.org/10.1038/ncomms15992

Chen, S., Hiraga, T., & Kohlstedt, D. L. (2006). Water weakening of clinopyroxene in the dislocation creep regime. *Journal of Geophysical Research: Solid Earth, 111*, B08203.

https://doi.org/10.1029/2005jb003885

Chen, W. P., & Molnar, P. (1983). Focal depths of intracontinental and intraplate earthquakes and their implications for the thermal and mechanical-properties of the lithosphere. *Journal of Geophysical Research, 88*(B5), 4183-4214. https://doi.org/10.1029/JB088iB05p04183

Cherniak, D. J. (2010). Diffusion in quartz, melilite, silicate perovskite, and mullite. *Reviews in Mineralogy and Geochemistry, 72*(1), 735-756. https://doi.org/10.2138/rmg.2010.72.16

Clark, M. K., Bush, J. W. M., & Royden, L. H. (2005). Dynamic topography produced by lower crustal flow against rheological strength heterogeneities bordering the Tibetan Plateau. *Geophysical Journal International, 162*(2), 575-590. https://doi.org/10.1111/j.1365-246X.2005.02580.x

Copley, A., Avouac, J. P., & Wernicke, B. P. (2011). Evidence for mechanical coupling and strong Indian lower crust beneath southern Tibet. *Nature, 472*(7341), 79-81. https://doi.org/10.1038/nature09926

Dimanov, A., & Dresen, G. (2005). Rheology of synthetic anorthite-diopside aggregates: Implications for ductile shear zones. *Journal of Geophysical Research: Solid Earth, 110*, B07203. https://doi.org/10.1029/2004jb003431

Dimanov, A., Dresen, G., Xiao, X., & Wirth, R. (1999). Grain boundary diffusion creep of synthetic anorthite aggregates: The effect of water. *Journal of Geophysical Research: Solid Earth, 104*(B5), 10483-10497. https://doi.org/10.1029/1998jb900113

Dimanov, A., Lavie, M. P., Dresen, G., Ingrin, J., & Jaoul, O. (2003). Creep of polycrystalline anorthite and diopside. *Journal of Geophysical Research: Solid Earth, 108*(B1), 2061. https://doi.org/10.1029/2002jb001815

Fan, W. M., Zhang, H. F., Baker, J., Jarvis, K. E., Mason, P. R. D., & Menzies, M. A. (2000). On and off the North China Craton: Where is the Archaean keel? *Journal of Petrology, 41*(7), 933-950. https://doi.org/10.1093/petrology/41.7.933

Farla, R., Rosenthal, A., Bollinger, C., Petitgirard, S., Guignard, J., Miyajima, N., et al. (2017). High-pressure, high-temperature deformation of dunite, eclogite, clinopyroxenite and garnetite using in situ X-ray diffraction. *Earth and Planetary Science Letters, 473*, 291-302. https://doi.org/10.1016/j.epsl.2017.06.019

Franěk, J., Schulmann, K., Lexa, O., Ulrich, S., Stipska, P., Haloda, J., et al. (2011). Origin of felsic granulite microstructure by heterogeneous decomposition of alkali feldspar and extreme weakening of orogenic lower crust during the Variscan orogeny. *Journal of Metamorphic Geology, 29*(1), 103-130. https://doi.org/10.1111/j.1525-1314.2010.00911.x

Gao, S., Rudnick, R. L., Yuan, H. L., Liu, X. M., Liu, Y. S., Xu, W. L., et al. (2004). Recycling lower continental crust in the North China craton. *Nature, 432*(7019), 892-897. https://doi.org/10.1038/nature03162

Gao, S., Zhang, B.-R., Jin, Z.-M., Kern, H., Ting-Chuan, L., & Zhao, Z.-D. (1998). How mafic is the lower continental crust? *Earth and Planetary Science Letters, 161*(1-4), 101-117. https://doi.org/10.1016/s0012-821x(98)00140-x

Gao, S., Zhang, J., Xu, W., & Liu, Y. (2009). Delamination and destruction of the North China Craton. *Chinese Science Bulletin, 54*(19), 3367-3378. https://doi.org/10.1007/s11434-009-0395-9

Gerbault, M., Martinod, J., & Hérail, G. (2005). Possible orogeny-parallel lower crustal flow and thickening in the Central Andes. *Tectonophysics, 399*, 59-72. https://doi.org/10.1016/j.tecto.2004.12.015

Green, H. W., & Borch, R. S. (1989). A new molten-salt cell for precision stress measurement at high-pressure. *European Journal of Mineralogy, 1*(2), 213-219. https://doi.org/10.1127/ejm/1/2/0213

Griffin, W. L., & O'Reilly, S. Y. (1986). The lower crust in eastern Australia: Xenolith evidence. In J. B. Dawson, D. A. Carswell, J. Hall, K. H. Wedepohl (Eds.), *The nature of the lower continental crust, Geological Society Special Publication* (Vol. 24, pp. 363-374). London: Blackwell Science Publications.

Griggs, D. T., & Blacic, J. D. (1965). Quartz: Anomalous weakness of synthetic crystals. *Science, 147*(3655), 292-295. https://doi.org/10.1126/science.147.3655.292

Hacker, B. R., Kelemen, P. B., & Behn, M. D. (2015). Continental lower crust. *Annual Review of Earth and Planetary Sciences, 43*(1), 167-205. https://doi.org/10.1146/annurev-earth-050212-124117

Hansen, L. N., Zimmerman, M. E., & Kohlstedt, D. L. (2012). Laboratory measurements of the viscous anisotropy of olivine aggregates. *Nature, 492*(7429), 415-418. https://doi.org/10.1038/nature11671

Hauri, E., Wang, J., Dixon, J. E., King, P. L., Mandeville, C., & Newman, S. (2002). SIMS analysis of volatiles in volcanic glasses, 1, Calibration, matrix effects and comparisons with FTIR. *Chemical Geology, 183*, 99-114.

Heidelbach, F., Post, A., & Tullis, J. (2000). Crystallographic preferred orientation in albite samples deformed experimentally by dislocation and solution precipitation creep. *Journal of Structural Geology, 22*(11-12), 1649-1661. https://doi.org/10.1016/S0191-8141(00)00072-9

Hirth, G., & Kohlstedt, D. (2003). Rheology of the upper mantle and the mantle wedge: A view from the experimentalists. In J. Eiler (Ed.), *Inside the subduction factory, Geophysical Monograph Series* (Vol. 138, pp. 83-105). Washington, DC: American Geophysical Union.

Homburg, J. M., Hirth, G., & Kelemen, P. B. (2010). Investigation of the strength contrast at the Moho: A case study from the Oman Ophiolite. *Geology, 38*(8), 679-682. https://doi.org/10.1130/G30880.1

Ito, Y., & Nakashima, S. (2002). Water distribution in low-grade siliceous metamorphic rocks by micro-FTIR and its relation to grain size: A case from the Kanto Mountain region, Japan. *Chemical Geology, 189*(1-2), 1-18. https://doi.org/10.1016/s0009-2541(02)00022-0

Jackson, J. (2002). Strength of the continental lithosphere: Time to abandon the jelly sandwich? *GSA Today, 12*(9), 4-9. https://doi.org/10.1130/1052-5173(2002)012<0004:sotclt>2.0.co;2

Ji, S. C., Jiang, Z. T., Rybacki, E., Wirth, R., Prior, D., & Xia, B. (2004). Strain softening and microstructural evolution of anorthite aggregates and quartz–anorthite layered composites deformed in torsion. *Earth and Planetary Science Letters, 222*(2), 377-390. https://doi.org/10.1016/j.epsl.2004.03.021

Ji, S. C., Long, C., Martignole, J., & Salisbury, M. (1997). Seismic reflectivity of a finely layered, granulite-facies ductile shear zone in the southern Grenville Province (Quebec). *Tectonophysics, 279*, 113-133.

Ji, S. C., Wirth, R., Rybacki, E., & Jiang, Z. T. (2000). High-temperature plastic deformation of quartz-plagioclase multilayers by layer-normal compression. *Journal of Geophysical Research: Solid Earth, 105*(B7), 16651-16664. https://doi.org/10.1029/2000jb900130

Ji, S. C., Zhao, P. L., & Xia, B. (2003). Flow laws of multiphase materials and rocks from end-member

flow laws. *Tectonophysics, 370*(1-4), 129-145. https://doi.org/10.1016/S0040-1951(03)00182-3

Johnson, E. A. (2006). Water in nominally anhydrous crustal minerals: Speciation, concentration, and geologic significance. *Reviews in Mineralogy and Geochemistry, 62*(1), 117-154. https://doi.org/10.2138/rmg.2006.62.6

Johnson, E. A., & Rossman, G. R. (2003). The concentration and speciation of hydrogen in feldspars using FTIR and ^{1}H MAS NMR spectroscopy. *American Mineralogist, 88*(5-6), 901-911. https://doi.org/10.2138/am-2003-5-620

Johnson, E. A., & Rossman, G. R. (2004). A survey of hydrous species and concentrations in igneous feldspars. *American Mineralogist, 89*(4), 586-600. https://doi.org/10.2138/am-2004-0413

Kohlstedt, D. L., Evans, B., & Mackwell, S. J. (1995). Strength of the lithosphere - Constraints imposed by laboratory experiments. *Journal of Geophysical Research: Solid Earth, 100*(B9), 17587-17602. https://doi.org/10.1029/95jb01460

Kovács, I., Hermann, J., O'Neill, H. St. C., Fitz Gerald, J., Sambridge, M., & Horvath, G. (2008). Quantitative absorbance spectroscopy with unpolarized light: Part II. Experimental evaluation and development of a protocol for quantitative analysis of mineral IR spectra. *American Mineralogist, 93*(5-6), 765-778. https://doi.org/10.2138/am.2008.2656

Kronenberg, A. K., & Wolf, G. H. (1990). Fourier transform infrared spectroscopy determinations of intragranular water content in quartz-bearing rocks: Implications for hydrolytic weakening in the laboratory and within the Earth. *Tectonophysics, 172*(3-4), 255-271. https://doi.org/10.1016/0040-1951(90)90034-6

Lund, M. D., Piazolo, S., & Harley, S. L. (2006). Ultrahigh temperature deformation microstructures in felsic granulites of the Napier Complex, Antarctica. *Tectonophysics, 427*(1-4), 133-151. https://doi.org/10.1016/j.tecto.2006.05.022

Martelat, J. E., Schulmann, K., Lardeaux, J. M., Nicollet, C., & Cardon, H. (1999). Granulite microfabrics and deformation mechanisms in southern Madagascar. *Journal of Structural Geology, 21*(6), 671-687. https://doi.org/10.1016/S0191-8141(99)00052-8

Mauler, A., Bystricky, M., Kunze, K., & Mackwell, S. (2000). Microstructures and lattice preferred orientations in experimentally deformed clinopyroxene aggregates. *Journal of Structural Geology,*

22(11-12), 1633-1648. https://doi.org/10.1016/S0191-8141(00)00073-0

Machek, M., Ulrich, S., & Janoušek, V. (2009). Strain coupling between upper mantle and lower crust: natural example from the Bestvina granulite body, Bohemian Massif. *Journal of Metamorphic Geology, 27*(9), 721-737.

Mehl, L., & Hirth, G. (2008). Plagioclase preferred orientation in layered mylonites: Evaluation of flow laws for the lower crust. *Journal of Geophysical Research: Solid Earth, 113*, B05202. https://doi.org/10.1029/2007jb005075

Mei, S., & Kohlstedt, D. L. (2000). Influence of water on plastic deformation of olivine aggregates: 2. Dislocation creep regime. *Journal of Geophysical Research: Solid Earth, 105*(B9), 21471-21481. https://doi.org/10.1029/2000jb900180

Meissner, R., & Mooney, W. (1998). Weakness of the lower continental crust: A condition for delamination, uplift, and escape. *Tectonophysics, 296*(1-2), 47-60. https://doi.org/10.1016/S0040-1951(98)00136-X

Meissner, R., Rabbel, W., & Kern, H. (2006). Seismic lamination and anisotropy of the lower continental crust. *Tectonophysics, 416*(1-4), 81-99. https://doi.org/10.1016/j.tecto.2005.11.013

Menzies, M. A., Fan, W., & Zhang, M. (1993). Palaeozoic and Cenozoic lithoprobes and the loss of >120 km of Archaean lithosphere, Sino-Korean craton, China. In H. M. Prichard, T. Alabaster, N. B. W. Harris, C. R. Neary (Eds.), *Magmatic processes and plate tectonics, Geological Society, London, Special Publications* (Vol. 76, pp. 71-81). Oxford: Alden Press.

Nakashima, S., Matayoshi, H., Yuko, T., Michibayashi, K., Masuda, T., Kuroki, N., et al. (1995). Infrared microspectroscopy analysis of water distribution in deformed and metamorphosed rocks. *Tectonophysics, 245*(3-4), 263-276. https://doi.org/10.1016/0040-1951(94)00239-6

O'Brien, P. J., & Rötzler, J. (2003). High-pressure granulites: formation, recovery of peak conditions and implications for tectonics. *Journal of Metamorphic Geology, 21*(1), 3-20. https://doi.org/10.1046/j.1525-1314.2003.00420.x

Passchier, C. W., & Trouw, R. A. J. (2005). *Microtectonics*. Berlin: Springer.

Peslier, A. H., Luhr, J. F., & Post, J. (2002). Low water contents in pyroxenes from spinel-peridotites of the oxidized, sub-arc mantle wedge. *Earth and Planetary Science Letters, 201*(1), 69-86.

https://doi.org/10.1016/S0012-821x(02)00663-5

Ranalli, G., & Murphy, D. C. (1987). Rheological stratification of the lithosphere. *Tectonophysics, 132*(4), 281-295. https://doi.org/10.1016/0040-1951(87)90348-9

Reyners, M., Eberhart-Phillips, D., & Stuart, G. (2007). The role of fluids in lower-crustal earthquakes near continental rifts. *Nature, 446*(7139), 1075-1078. https://doi.org/10.1038/nature05743

Ross, A. R., Brown, L. D., Pananont, P., Nelson, K. D., Klemperer, S., Haines, S., et al. (2004). Deep reflection surveying in central Tibet: Lower-crustal layering and crustal flow. *Geophysical Journal International, 156*(1), 115-128. https://doi.org/10.1111/j.1365-246X.2004.02119.x

Rossman, G. R. (1996). Studies of OH in nominally anhydrous minerals. *Physics and Chemistry of Minerals, 23*(4-5), 299-304. https://doi.org/10.1007/bf00207777

Royden, L. (1996). Coupling and decoupling of crust and mantle in convergent orogens: Implications for strain partitioning in the crust. *Journal of Geophysical Research: Solid Earth, 101*(B8), 17679-17705. https://doi.org/10.1029/96jb00951

Royden, L. H., Burchfiel, B. C., King, R. W., Wang, E., Chen, Z., Shen, F., et al. (1997). Surface deformation and lower crustal flow in eastern Tibet. *Science, 276*(5313), 788-790. https://doi.org/10.1126/science.276.5313.788

Rudnick, R. L., & Fountain, D. M. (1995). Nature and composition of the continental-crust - A lower crustal perspective. *Reviews of Geophysics, 33*(3), 267-309. https://doi.org/10.1029/95rg01302

Rudnick, R. L., & Gao, S. (2003). Composition of the continental crust. In R. L. Rudnick (Ed.), *The crust, Treatise on Geochemistry* (Vol. 3, pp. 1-64). Amsterdam: Elsevier.

Rutter, E. H., & Brodie, K. H. (2004). Experimental intracrystalline plastic flow in hot-pressed synthetic quartzite prepared from Brazilian quartz crystals. *Journal of Structural Geology, 26*(2), 259-270. https://doi.org/10.1016/S0191-8141(03)00096-8

Rybacki, E., & Dresen, G. (2000). Dislocation and diffusion creep of synthetic anorthite aggregates. *Journal of Geophysical Research: Solid Earth, 105*(B11), 26017-26036. https://doi.org/10.1029/2000jb900223

Rybacki, E., Gottschalk, M., Wirth, R., & Dresen, G. (2006). Influence of water fugacity and activation volume on the flow properties of fine-grained anorthite aggregates. *Journal of Geophysical*

Research: Solid Earth, 111, B03203. https://doi.org/10.1029/2005jb003663

Shapiro, N. M., Ritzwoller, M. H., Molnar, P., & Levin, V. (2004). Thinning and flow of Tibetan crust constrained by seismic anisotropy. *Science, 305*(5681), 233-236. https://doi.org/10.1126/science.1098276

Shi, F., Wang, Y., Yu, T., Zhu, L., Zhang, J., Wen, J., et al. (2018). Lower-crustal earthquakes in southern Tibet are linked to eclogitization of dry metastable granulite. *Nature Communications, 9*(1), 3483. https://doi.org/10.1038/s41467-018-05964-1

Skemer, P., Katayama, B., Jiang, Z. T., & Karato, S. (2005). The misorientation index: Development of a new method for calculating the strength of lattice-preferred orientation. *Tectonophysics, 411*(1-4), 157-167. https://doi.org/10.1016/j.tecto.2005.08.023

Skogby, H., Bell, D. R., & Rossman, G. R. (1990). Hydroxide in pyroxene: Variations in the natural environment. *American Mineralogist, 75*(7-8), 764-774.

Thomas, S. M., Koch-Muller, M., Reichart, P., Rhede, D., Thomas, R., Wirth, R., et al. (2009). IR calibrations for water determination in olivine, r-GeO_2, and SiO_2 polymorphs. *Physics and Chemistry of Minerals, 36*(9), 489-509. https://doi.org/10.1007/s00269-009-0295-1

Tullis, T. E., Horowitz, F. G., & Tullis, J. (1991). Flow laws of polyphase aggregates from end-member flow laws. *Journal of Geophysical Research, 96*(B5), 8081-8096. https://doi.org/10.1029/90jb02491

Wang, Y. F., Zhang, J. F., Jin, Z. M., & Green, H. W. (2012). Mafic granulite rheology: Implications for a weak continental lower crust. *Earth and Planetary Science Letters, 353-354*, 99-107. https://doi.org/10.1016/j.epsl.2012.08.004

Whitney, D. L., & Evans, B. W. (2010). Abbreviations for names of rock-forming minerals. *American Mineralogist, 95*(1), 185-187. https://doi.org/10.2138/am.2010.3371

Wilks, K. R., & Carter, N. L. (1990). Rheology of some continental lower crustal rocks. *Tectonophysics, 182*(1-2), 57-77. https://doi.org/10.1016/0040-1951(90)90342-6

Withers, A. C. (2013). On the use of unpolarized infrared spectroscopy for quantitative analysis of absorbing species in birefringent crystals. *American Mineralogist, 98*(4), 689-697. https://doi.org/10.2138/am.2013.4316

819 Xia, Q., Yang, X., Deloule, E., Sheng, Y.-M., & Hao, Y.-T. (2006). Water in the lower crustal granulite
820 xenoliths from Nushan, eastern China. *Journal of Geophysical Research: Solid Earth, 111*,
821 B11202. https://doi.org/10.1029/2006jb004296
822 Xie, Y. X., Wenk, H. R., & Matthies, S. (2003). Plagioclase preferred orientation by TOF neutron
823 diffraction and SEM-EBSD. *Tectonophysics, 370*(1-4), 269-286.
824 https://doi.org/10.1016/S0040-1951(03)00191-4
825 Xu, W. L., Gao, S., Wang, Q. H., Wang, D. Y., & Liu, Y. S. (2006). Mesozoic crustal thickening of the
826 eastern North China craton: Evidence from eclogite xenoliths and petrologic implications.
827 *Geology, 34*(9), 721-724. https://doi.org/10.1130/G22551.1
828 Xu, W. L., Wang, D., Liu, X., Wang, Q., & Lin, J. (2002). Discovery of eclogite inclusions and its
829 geological significance in early Jurassic intrusive complex in Xuzhounorthern Anhui, eastern
830 China. *Chinese Sci Bull, 47*(14), 1212-1216. https://doi.org/10.1007/bf02907612
831 Xu, Y. G. (2001). Thermo-tectonic destruction of the Archaean lithospheric keel beneath the
832 Sino-Korean Craton in China: Evidence, timing and mechanism. *Physics and Chemistry of the*
833 *Earth Part a-Solid Earth and Geodesy, 26*(9-10), 747-757.
834 https://doi.org/10.1016/S1464-1895(01)00124-7
835 Yang, C., & Wei, C. J. (2017). Ultrahigh temperature (UHT) mafic granulites in the East Hebei, North
836 China Craton: Constraints from a comparison between temperatures derived from REE-based
837 thermometers and major element-based thermometers. *Gondwana Research, 46*, 156-169.
838 https://doi.org/10.1016/j.gr.2017.02.017
839 Yang, X., Deloule, E., Xia, Q., Fan, Q.-C., & Feng, M. (2008). Water contrast between Precambrian
840 and Phanerozoic continental lower crust in eastern China. *Journal of Geophysical Research: Solid*
841 *Earth, 113*, B08207. https://doi.org/10.1029/2007jb005541
842 Zhang, J., & Green, H. W. (2007). Experimental investigation of eclogite rheology and its fabrics at
843 high temperature and pressure. *Journal of Metamorphic Geology, 25*(2), 97-115.
844 https://doi.org/10.1111/j.1525-1314.2006.00684.x
845 Zhao, Y. H., Ginsberg, S. B., & Kohstedt, D. L. (2004). Solubility of hydrogen in olivine: dependence
846 on temperature and iron content. *Contributions to Mineralogy and Petrology, 147*(2), 155-161.

847 https://doi.org/10.1007/s00410-003-0524-4

848

FIGURE CAPTIONS

Figure 1. Microphotographs showing the typical shape of hot-pressed and deformed samples cutting along their longitudinal sections. (a) Hot-pressed (sample GA289); (b) Deformed (sample GA370). It can be inferred from these cross-sectional shapes that both the hot-pressed and the deformed samples should be nearly cylindrical.

Figure 2. Mechanical results of high-temperature creep of felsic granulite. (a) Typical stress-strain curves. Note that a steady-state deformation is generally reached after a strain of about 20%. (b) Log-log plot of strain rate versus stress for the steady-state flow of felsic granulite at 827 ºC, 877 ºC and 927 ºC, yielding a stress exponents of $n = 4.2 \pm 0.1$ and a pre-exponential factor of $A = 10^{-4.4 \pm 0.2}$ $MPa^{-4.2}s^{-1}$. (c) Semi-log plot of stress versus inverse temperature for constant strain rates of 9.4×10^{-5} s^{-1}, 1.1×10^{-5} s^{-1} and 3.6×10^{-6} s^{-1}, yielding an activation energy of $Q = 260 \pm 30$ kJ/mol.

Figure 3. Representative microstructures of hot-pressed (a, b) and deformed (c, d) felsic granulite samples. (a and b) The hot-pressed sample (GA279) was annealed under a pressure of 1 GPa and 927 ºC for 12 h. A weak SPO of aligned elongate pyroxene and amphibole grains can be discerned. (c and d) A more pronounced SPO of elongated pyroxene and amphibole, and sometimes quartz can be observed in a deformed sample (GA370). The green opposite arrows represent the longitudinal shortening direction during hot-pressing and deformation. (a and c) Backscattered electron images; (b and d) Photomicrographs in cross-polarized light. All scale bars are 100 μm. Mineral abbreviations here and hereinafter are after Whitney and Evans (2010).

Figure 4. Crystallographic preferred orientations of clinopyroxene, orthopyroxene, plagioclase, and quartz from a hot-pressed (a), and three deformed (b, c, and d) felsic granulite samples. Pole figures are lower hemisphere equal area projections and

877 contoured with a half width of 20° and a cluster size of 5°. For the hot-pressed sample,
878 the longitudinal shortening direction (as indicated by the green opposite arrows) is
879 vertical in each pole figure. For the deformed samples, the foliation plane (S) is E-W
880 and normal to the paper in each pole figure. The contour interval is one multiple of
881 uniform distribution. *n*, number of measured grains; *J*, J-index; *M*, M-index; U,
882 upper-hemisphere projection; L, lower-hemisphere projection.
883
884 **Figure 5.** EBSD mappings showing intracrystalline deformation features (subgrain
885 structure) in (a) plagioclase, (b) clinopyroxene, (c) orthopyroxene, and (d) quartz.
886
887 **Figure 6**. SEM micrographs showing typical grain boundaries of quartz with other
888 minerals and triple junctions among plagioclase, quartz and pyroxene in the deformed
889 samples at high magnifications. No melt is clearly visible along the grain boundaries
890 and triple junctions with these magnifications.
891
892 **Figure 7.** Compositional mapping of Si, Al, Fe, Mg, and Ca in a deformed felsic
893 granulite. Warmer or brighter colors indicate higher concentrations. Color scales in
894 different X-ray maps do not correspond to the same element concentration. Note the
895 clear-cut grain/phase boundaries and the absence of compositional zoning in minerals.
896
897 **Figure 8.** Representative FTIR spectra of plagioclase (a), quartz (b), clinopyroxene
898 (c), and orthopyroxene (d) from the starting material. All spectra were normalized to 1
899 cm thickness and offset vertically for clarity.
900
901 **Figure 9.** Flow strength comparison of felsic granulite in this study (black dashed
902 lines) with common crustal mineral aggregates (a) and other granulites (b) in the
903 dislocation creep regime by extrapolating flow laws to a natural strain rate of 10^{-14} s^{-1}.
904 Flow laws: wet and dry anorthite aggregates (Rybacki & Dresen, 2000); wet quartz

aggregates (Rutter & Brodie, 2004); wet clinopyroxene aggregates (Chen et al., 2006); wet enstatite aggregates (Bystricky et al., 2016); felsic and mafic granulite (WC1990) (Wilks & Carter, 1990).

Figure 10. Comparison of flow strength of our felsic granulite (black solid line) with those of eclogite and olivine aggregates in the dislocation creep regime by extrapolating flow laws to a natural strain rate of 10^{-14} s^{-1}. Mafic granulite from Wang et al. (2012) is also shown to facilitate comparison. Flow laws for eclogite and dry/wet olivine aggregates are taken from Zhang and Green (2007) and Hirth and Kohlstedt (2003), respectively. The water concentration (~ 57 wt ppm H_2O) for wet olivine aggregates was estimated using the water solubility equation of olivine from Zhao et al. (2004) by assuming a fayalite number (X_{Fa}) of 0.1 under a pressure of 1 GPa and a temperature of 900 ºC. This water concentration represents the maximum water concentration that can be incorporated into olivine close to the Moho.

Figure 1.

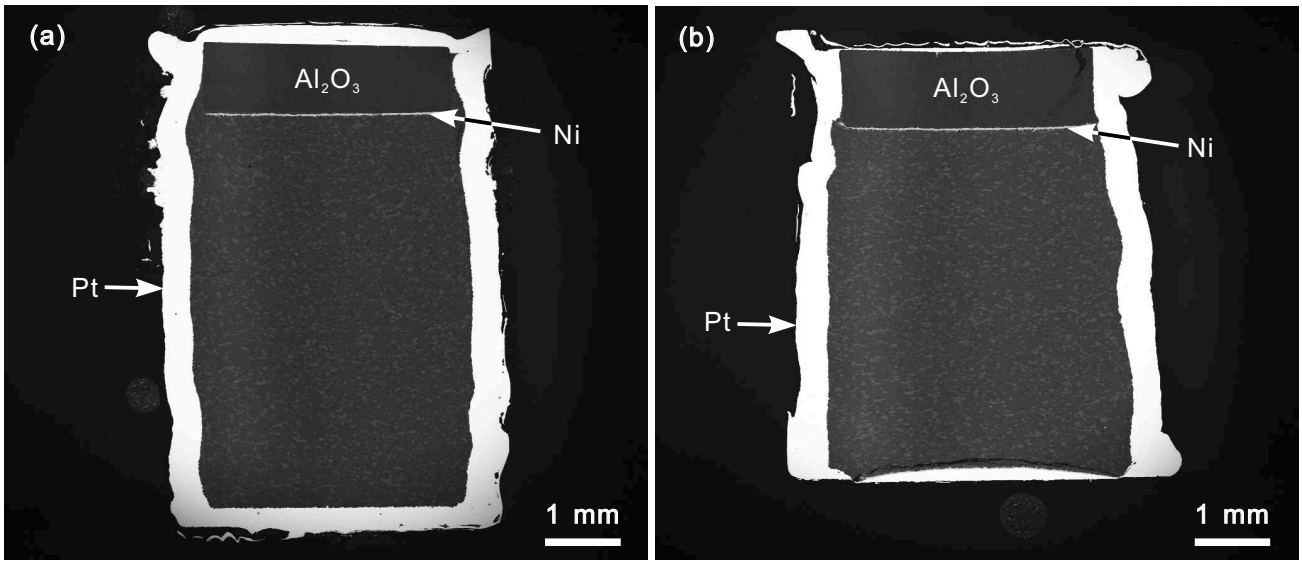
(a)
Al_2O_3
Ni
Pt
1 mm
(b)
Al_2O_3
Ni
Pt
1 mm

Figure 2.

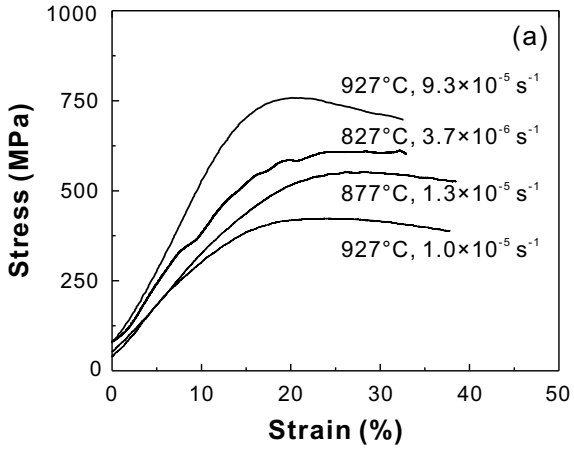
(a)
927°C, 9.3×10^-5 s^-1
827°C, 3.7×10^-6 s^-1
877°C, 1.3×10^-5 s^-1
927°C, 1.0×10^-5 s^-1
Stress (MPa)
Strain (%)
1000
750
500
250
0
0
10
20
30
40
50

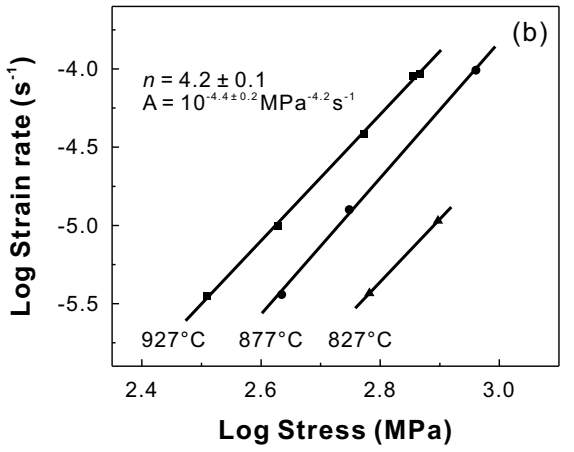
(b)
n = 4.2 ± 0.1
A = 10^-4.4±0.2 MPa^-4.2 s^-1
927°C
877°C
827°C
Log Strain rate (s^-1)
Log Stress (MPa)
-4.0
-4.5
-5.0
-5.5
2.4
2.6
2.8
3.0

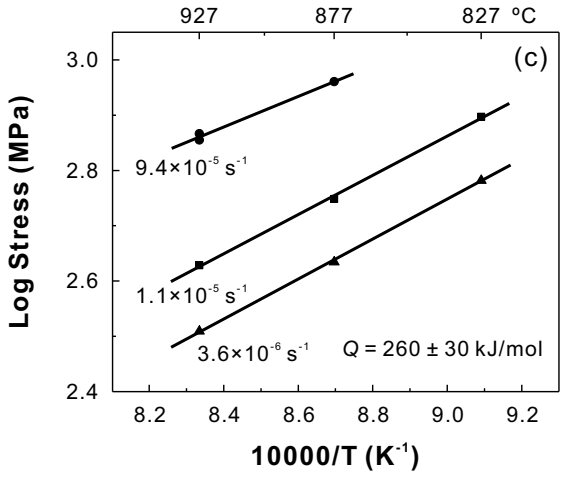
927
877
827 ºC
(c)
9.4×10^-5 s^-1
1.1×10^-5 s^-1
3.6×10^-6 s^-1
Q = 260 ± 30 kJ/mol
Log Stress (MPa)
10000/T (K^-1)
3.0
2.8
2.6
2.4
8.2
8.4
8.6
8.8
9.0
9.2

Figure 3.

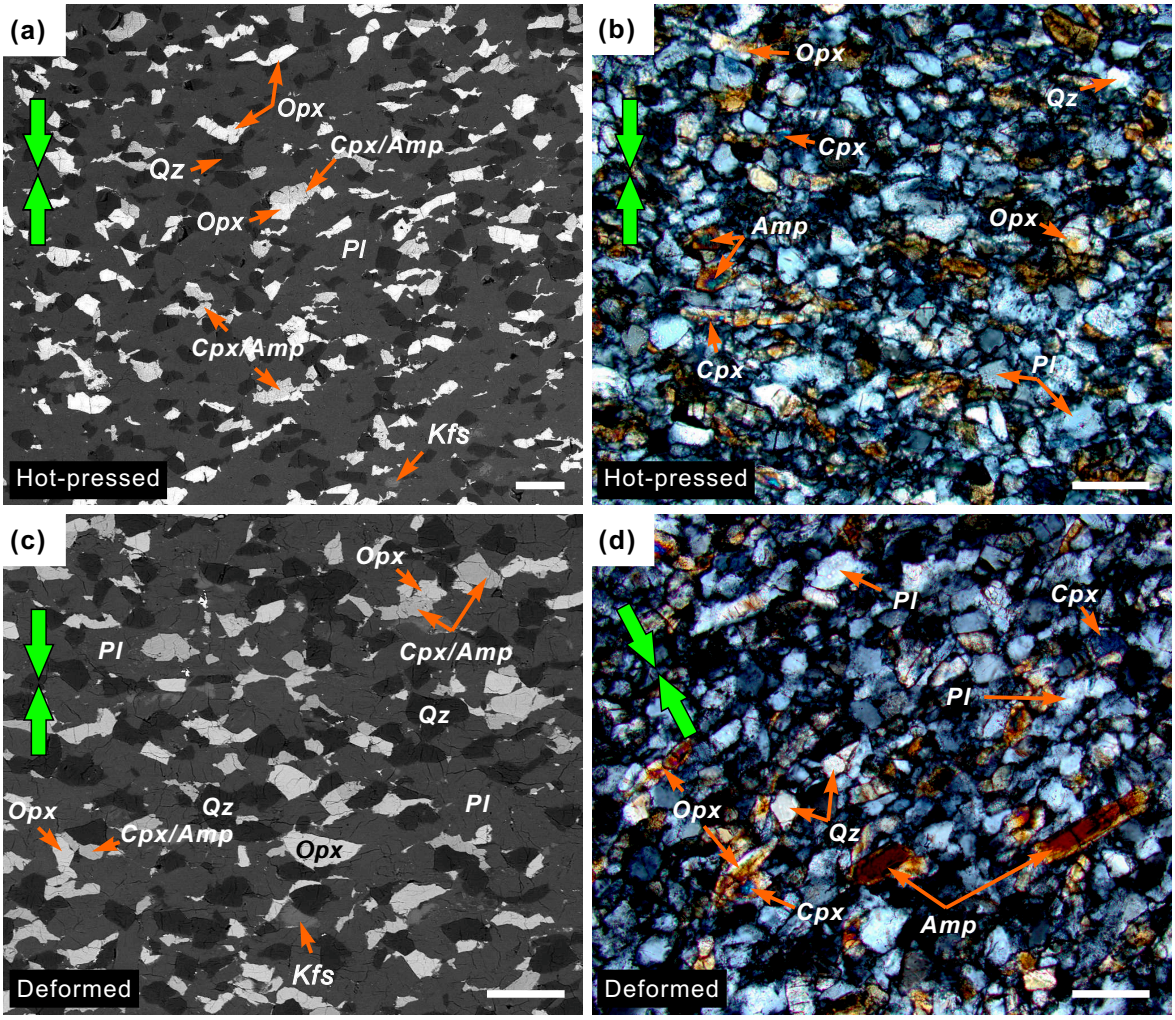
(a)
Opx
Qz
Cpx/Amp
Opx
Pl
Cpx/Amp
Kfs
Hot-pressed
(b)
Opx
Qz
Cpx
Amp
Opx
Cpx
Pl
Hot-pressed
(c)
Opx
Pl
Cpx/Amp
Qz
Opx
Qz
Cpx/Amp
Pl
Opx
Kfs
Deformed
(d)
Pl
Cpx
Pl
Opx
Qz
Cpx
Amp
Deformed

Figure 4.

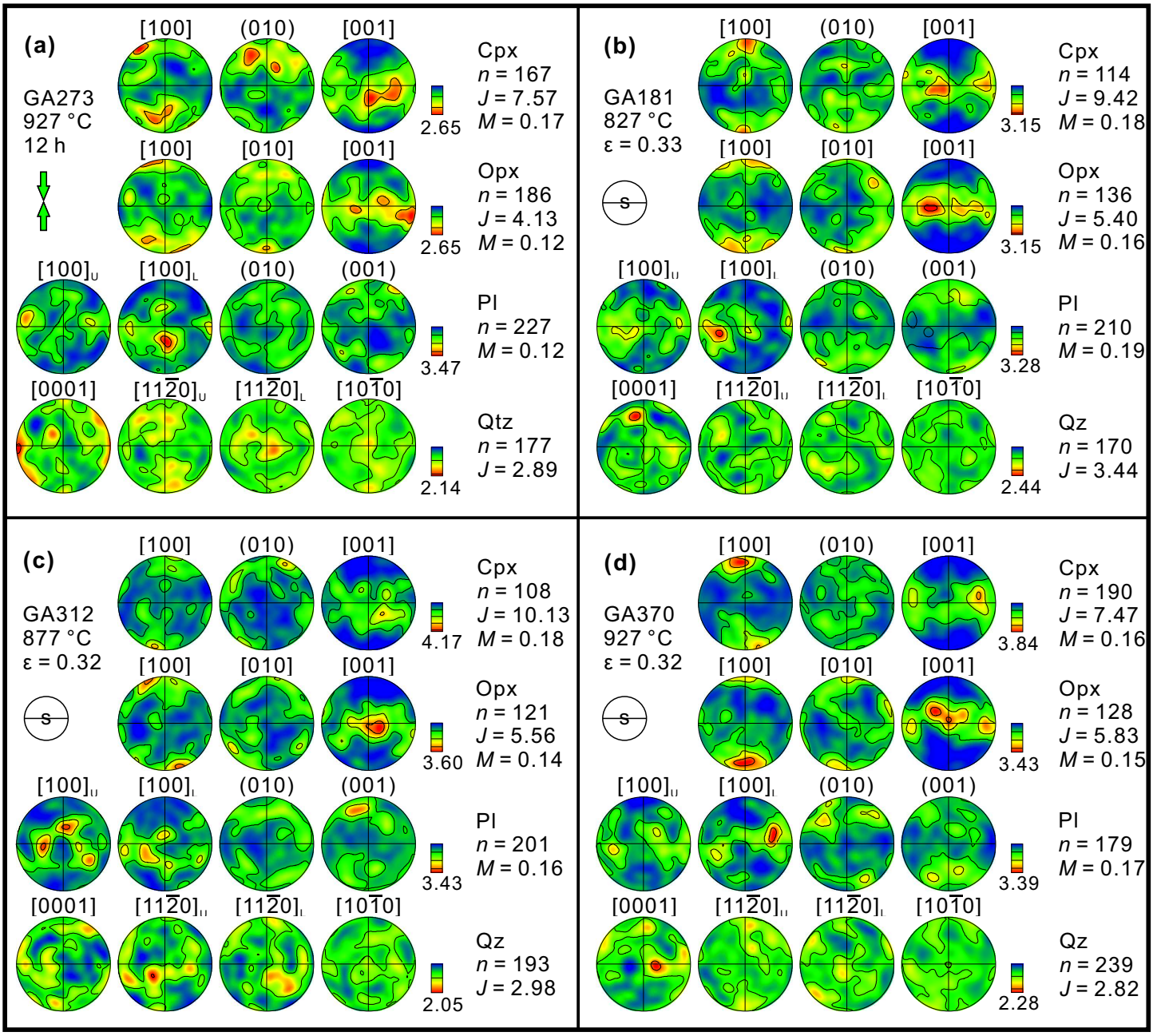
(a)
GA273
927 °C
12 h
[100]
(010)
[001]
2.65
Cpx
n = 167
J = 7.57
M = 0.17
[100]
[010]
[001]
2.65
Opx
n = 186
J = 4.13
M = 0.12
[100]U
[100]L
(010)
(001)
3.47
Pl
n = 227
M = 0.12
[0001]
[11$\bar{2}$0]U
[11$\bar{2}$0]L
[10$\bar{1}$0]
2.14
Qtz
n = 177
J = 2.89
(b)
GA181
827 °C
ε = 0.33
S
[100]
(010)
[001]
3.15
Cpx
n = 114
J = 9.42
M = 0.18
[100]
[010]
[001]
3.15
Opx
n = 136
J = 5.40
M = 0.16
[100]U
[100]L
(010)
(001)
3.28
Pl
n = 210
M = 0.19
[0001]
[11$\bar{2}$0]U
[11$\bar{2}$0]L
[10$\bar{1}$0]
2.44
Qz
n = 170
J = 3.44
(c)
GA312
877 °C
ε = 0.32
S
[100]
(010)
[001]
4.17
Cpx
n = 108
J = 10.13
M = 0.18
[100]
[010]
[001]
3.60
Opx
n = 121
J = 5.56
M = 0.14
[100]U
[100]L
(010)
(001)
3.43
Pl
n = 201
M = 0.16
[0001]
[11$\bar{2}$0]U
[11$\bar{2}$0]L
[10$\bar{1}$0]
2.05
Qz
n = 193
J = 2.98
(d)
GA370
927 °C
ε = 0.32
S
[100]
(010)
[001]
3.84
Cpx
n = 190
J = 7.47
M = 0.16
[100]
[010]
[001]
3.43
Opx
n = 128
J = 5.83
M = 0.15
[100]U
[100]L
(010)
(001)
3.39
Pl
n = 179
M = 0.17
[0001]
[11$\bar{2}$0]U
[11$\bar{2}$0]L
[10$\bar{1}$0]
2.28
Qz
n = 239
J = 2.82

Figure 5.

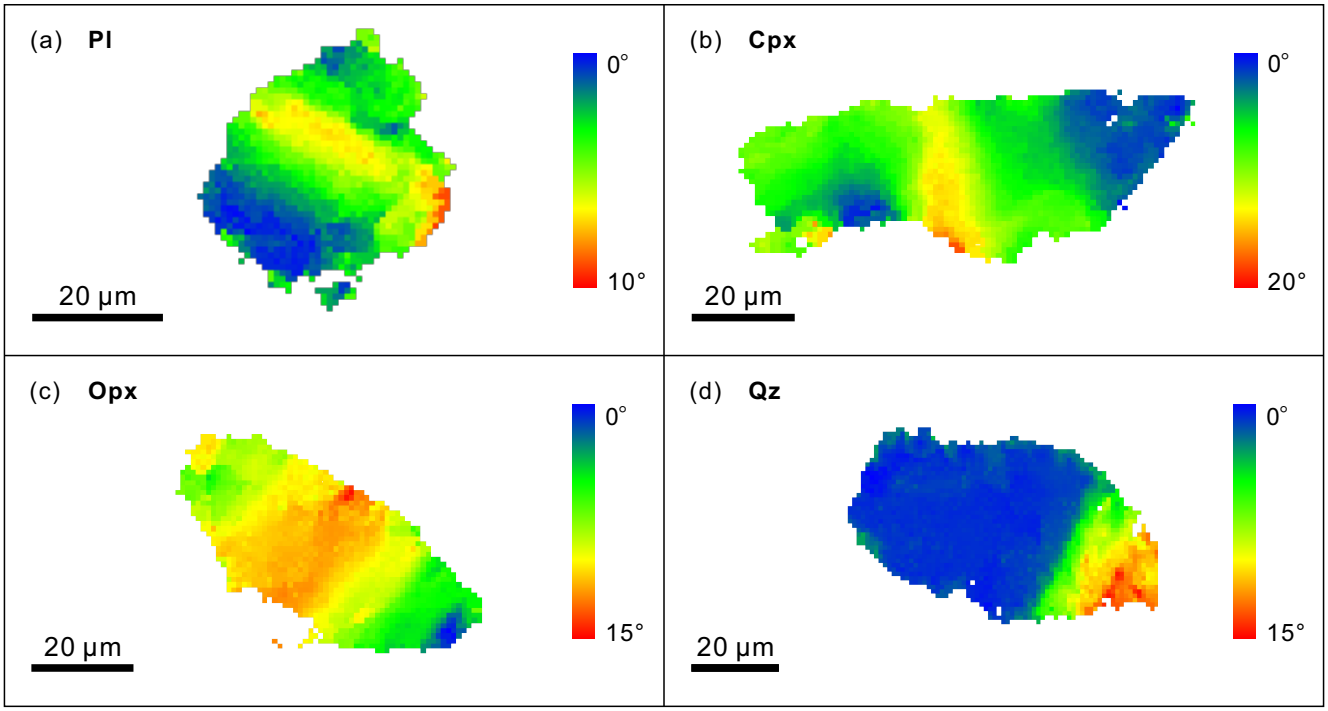
(a) Pl
0°
10°
20 μm
(b) Cpx
0°
20°
20 μm
(c) Opx
0°
15°
20 μm
(d) Qz
0°
15°
20 μm

Figure 6.

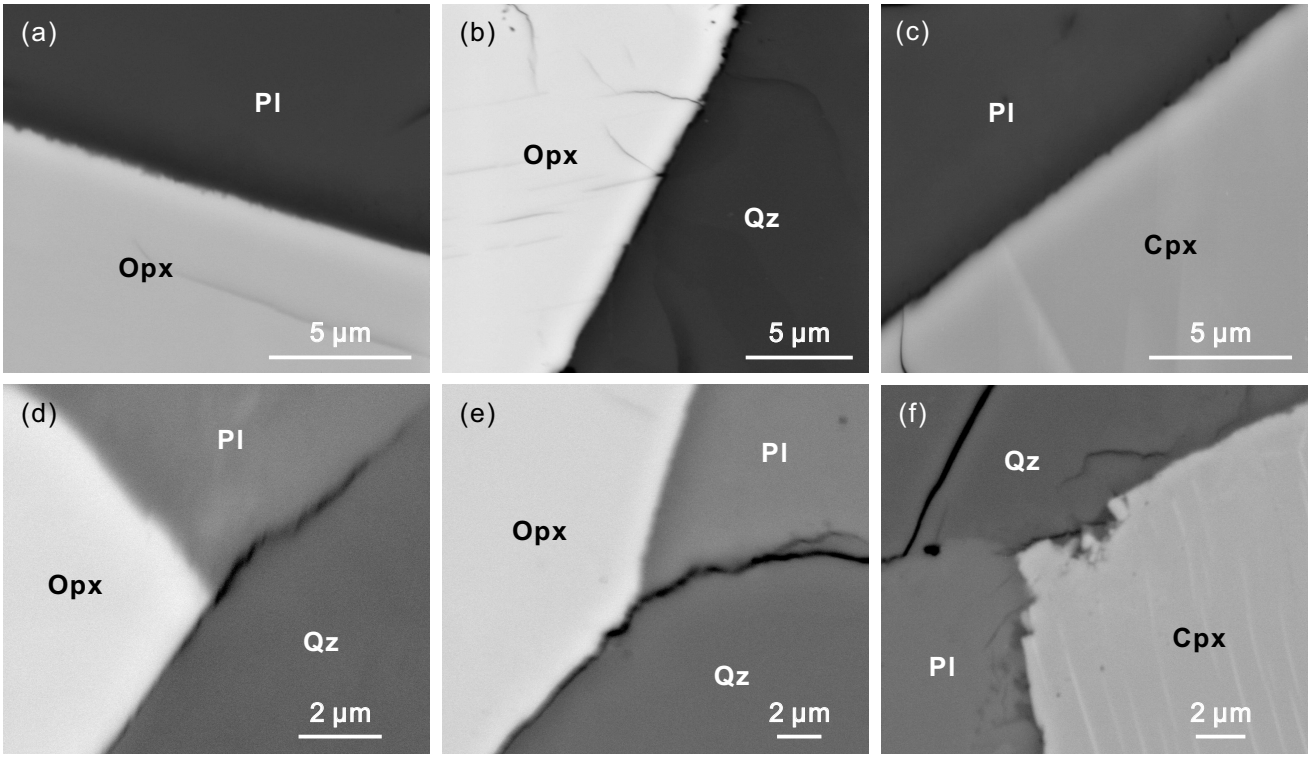
(a)
Pl
Opx
5 μm
(b)
Opx
Qz
5 μm
(c)
Pl
Cpx
5 μm
(d)
Pl
Opx
Qz
2 μm
(e)
Pl
Opx
Qz
2 μm
(f)
Qz
Cpx
Pl
2 μm

Figure 7.

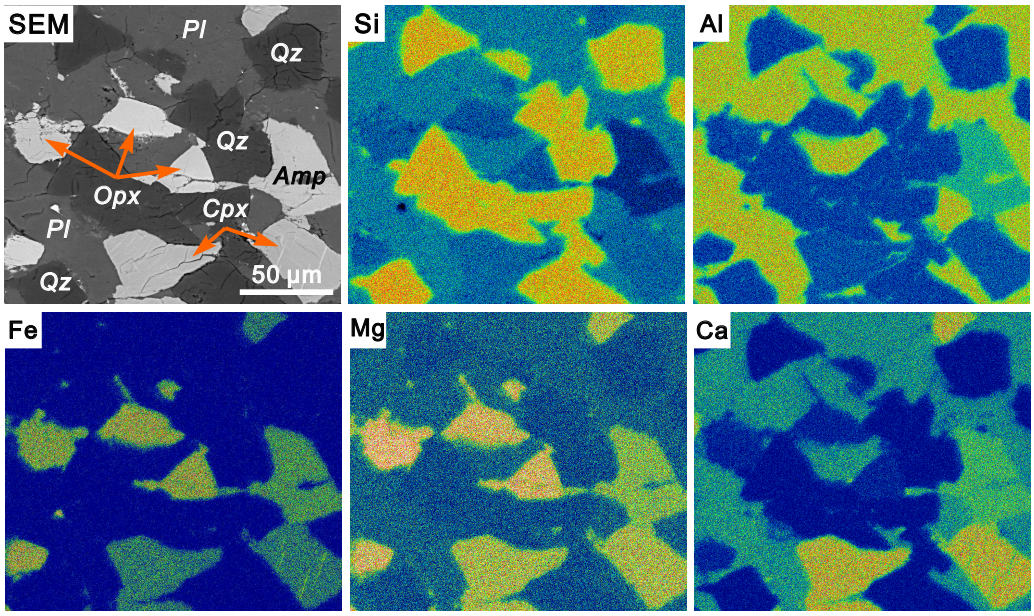
SEM
Pl
Qz
Qz
Amp
Opx
Cpx
Pl
Qz
50 µm
Si
Al
Fe
Mg
Ca

Figure 8.

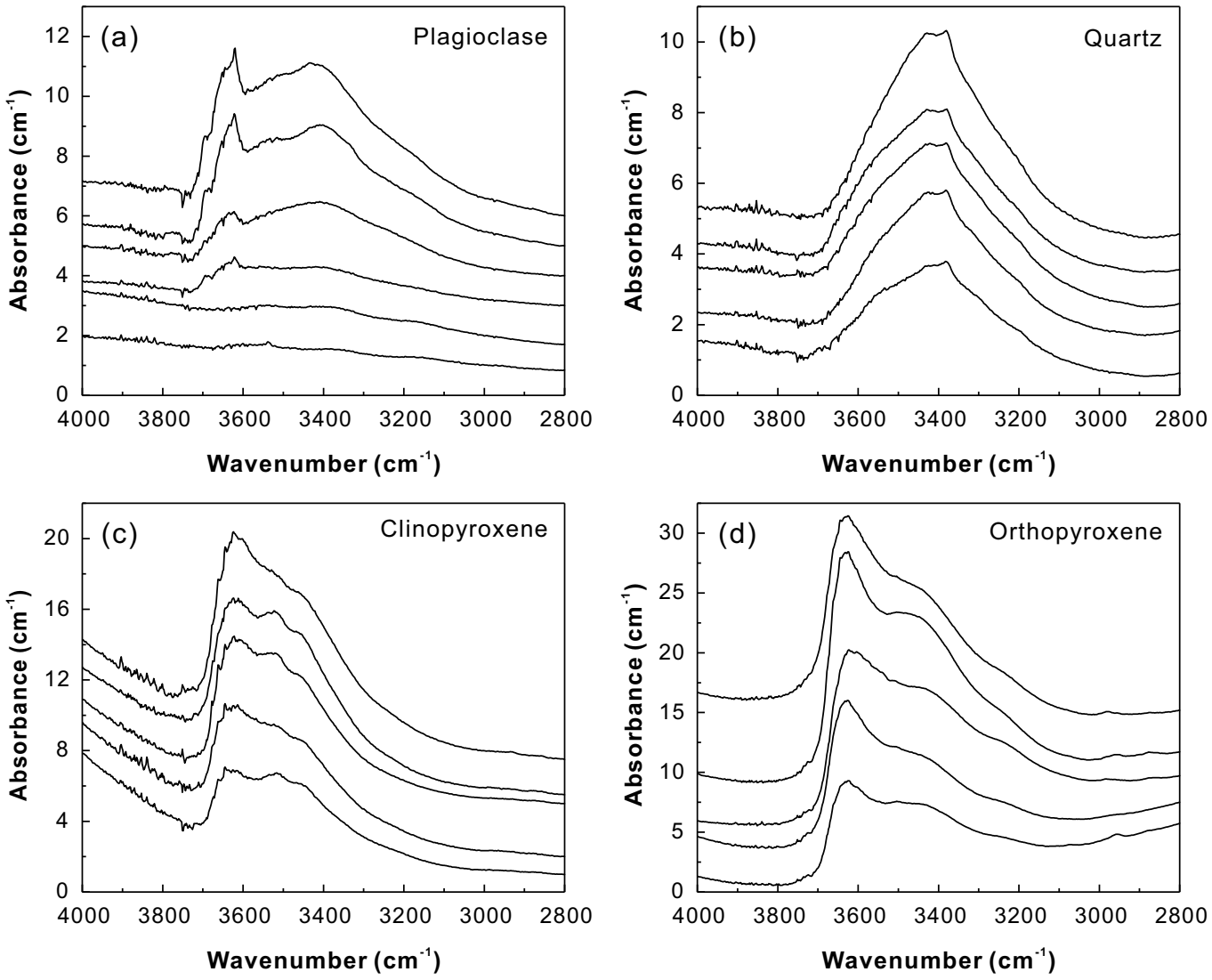
(a)
Plagioclase
Absorbance (cm-1)
Wavenumber (cm-1)
(b)
Quartz
Absorbance (cm-1)
Wavenumber (cm-1)
(c)
Clinopyroxene
Absorbance (cm-1)
Wavenumber (cm-1)
(d)
Orthopyroxene
Absorbance (cm-1)
Wavenumber (cm-1)

Figure 9.

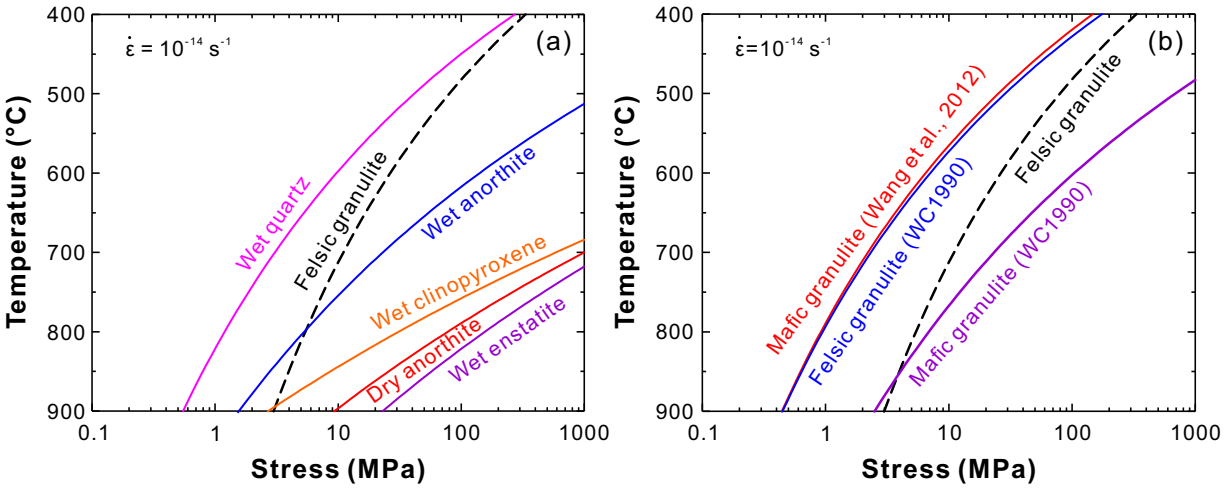
(a)
$\dot{\varepsilon}$ = 10^{-14} s^{-1}
Wet quartz
Felsic granulite
Wet anorthite
Wet clinopyroxene
Dry anorthite
Wet enstatite
Temperature (°C)
Stress (MPa)
400
500
600
700
800
900
0.1
1
10
100
1000
(b)
$\dot{\varepsilon}$=10^{-14} s^{-1}
Mafic granulite (Wang et al., 2012)
Felsic granulite (WC1990)
Felsic granulite
Mafic granulite (WC1990)
Temperature (°C)
Stress (MPa)

Figure 10.

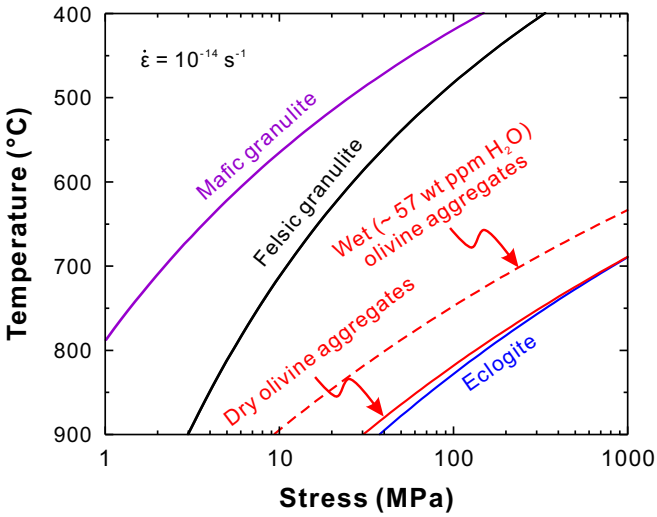
400
500
600
700
800
900
1
10
100
1000
Temperature (°C)
Stress (MPa)
$\dot{\varepsilon}$ = 10^{-14} s^{-1}
Mafic granulite
Felsic granulite
Wet (~ 57 wt ppm H_2O) olivine aggregates
Dry olivine aggregates
Eclogite

Table 1.
Experimental Conditions and Mechanical Data for Felsic Granulite

Expt. #	P (GPa)	T (°C)	R or ε (%)[a]	$\dot{\varepsilon}$ (s^{-1})	σ (MPa)
Hot-pressing Experiments					
GA273	1	927	35	-	-
GA279	1	927	37	-	-
GA283	1	927	38	-	-
Deformation Experiments					
GA331	1	927	34	3.6×10^{-6}	323
GA321	1	927	38	1.0×10^{-5}	425
GA139	1	927	49	3.8×10^{-5}	592
GA327	1	927	42	9.0×10^{-5}	716
GA370	1	927	33	9.3×10^{-5}	735
GA317	1	877	37	9.8×10^{-5}	913
GA312	1	877	38	1.3×10^{-5}	560
GA206	1	877	36	3.6×10^{-6}	431
GA181	1	827	33	3.7×10^{-6}	605
GA161	1	827	33	1.1×10^{-5}	789

[a]Axial compression ratio and strain for deformed and hot-pressed samples, respectively.

Table 2.

Chemical Compositions (wt%) of Major Minerals in the Starting Material and Selected Hot-pressed and Deformed Granulite

Sample	Mineral	SiO_2	TiO_2	Al_2O_3	Cr_2O_3	FeO	MnO	MgO	CaO	Na_2O	K_2O	Total	End Member
09TPZ-1 Starting material	Pl	61.09	0.02	23.56	-	0.09	0.01	-	6.83	7.20	0.47	99.28	$An_{33}Ab_{64}Or_3$
	Cpx	52.42	0.14	2.09	0.01	11.38	0.37	11.92	20.41	0.64	0.01	99.34	$Wo_{45}En_{36}Fs_{19}$
	Opx	51.74	0.06	1.24	0.02	27.79	0.81	17.05	0.59	0.03	0.01	99.42	$Wo_1En_{52}Fs_{47}$
	Amp	42.29	2.24	11.18	0.03	16.28	0.17	9.87	10.93	1.39	1.85	96.25	
GA283 Hot-pressed	Pl	60.18	0.04	24.29	-	0.13	0.02	0.01	7.65	6.30	0.65	99.28	$An_{39}Ab_{57}Or_{04}$
	Cpx	52.50	0.22	1.94	0.02	11.63	0.38	11.66	20.50	0.47	0.01	99.35	$Wo_{45}En_{36}Fs_{19}$
	Opx	52.27	0.07	0.92	0.03	27.32	0.68	17.62	0.59	0.03	0.01	99.53	$Wo_1En_{53}Fs_{46}$
	Amp	42.35	2.55	10.90	0.07	17.78	0.19	8.95	11.12	1.45	1.94	97.31	
GA161 Deformed	Pl	60.30	0.04	24.39	-	0.19	0.01	0.01	7.51	6.36	0.53	99.35	$An_{38}Ab_{59}Or_3$
	Cpx	52.63	0.22	1.99	0.03	11.74	0.36	11.50	20.38	0.51	0.00	99.38	$Wo_{45}En_{35}Fs_{20}$
	Opx	52.66	0.10	0.99	0.04	26.18	0.65	17.98	0.66	0.01	0.01	99.29	$Wo_1En_{54}Fs_{45}$
	Amp	43.03	2.19	11.19	0.01	18.02	0.18	8.76	11.12	1.23	1.86	97.59	
GA370 Deformed	Pl	59.78	-	24.70	0.01	0.20	-	-	7.83	6.23	0.48	99.24	$An_{40}Ab_{57}Or_3$
	Cpx	52.17	0.22	1.98	0.02	12.04	0.34	11.63	20.43	0.48	0.01	99.31	$Wo_{45}En_{35}Fs_{20}$
	Opx	51.48	0.11	0.94	0.05	27.75	0.58	17.50	0.67	0.02	0.01	99.12	$Wo_1En_{53}Fs_{46}$
	Amp	43.40	1.80	12.02	0.01	14.82	0.16	10.18	11.40	1.24	1.95	96.98	

"-", under detection limit.

Table 3.

Summary of FTIR Results for Major Component Minerals in the Starting Material

Mineral	Measured Grains	A_i (cm^{-1})[a]		C_{H2O} (wt ppm)	
		Range	Average[b]	Range	Average[b]
Pl	15	2.0-46.1	24.0 ± 14.4	17-401	209 ± 126
Qz	11	21.0-64.5	35.9 ± 12.9	208-636	355 ± 127
Cpx	11	10.3-97.8	49.8 ± 27.7	193-1839	937 ± 521
Opx	12	51.1-248.2	126.1 ± 61.8	459-2229	1132 ± 555

[a]A_i represents the absolute integrated absorbance.

[b]Errors represent one standard deviation.